Joule

CellPress

Article

Solution-Processed All-Perovskite Multi-Junction Solar Cells

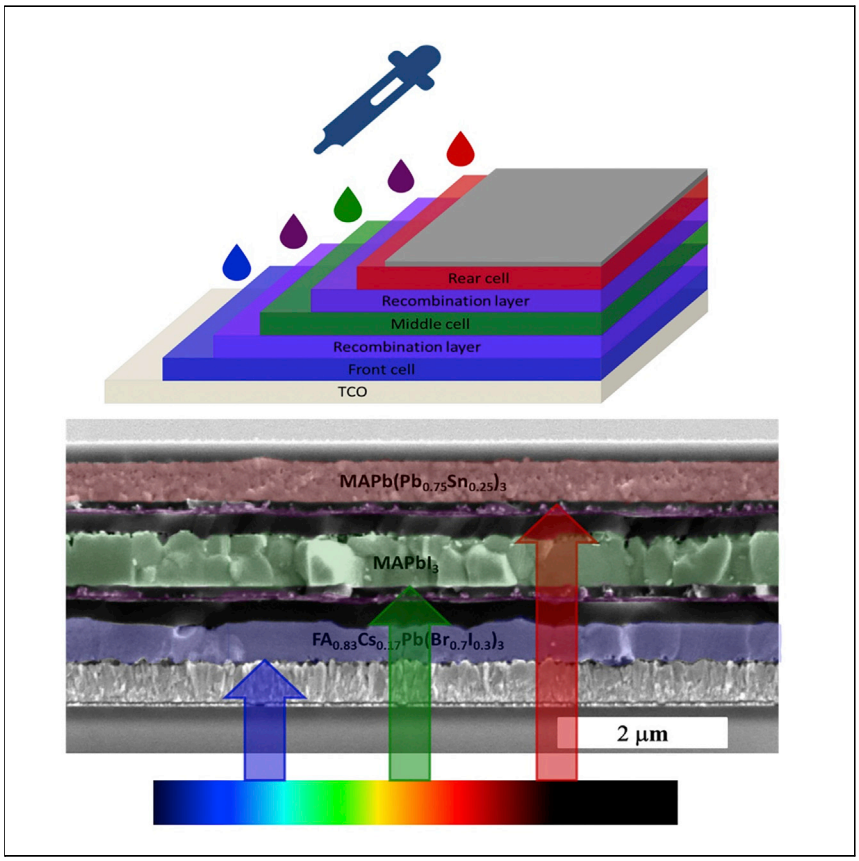

Perovskite solar cells can be processed using solution-based methods. Furthermore, perovskite solar cells can tune their band gap to absorb different portions of the solar spectrum. This property allows for fabrication of multi-junction solar cell, which can offer higher power conversion efficiencies than single-junction architecture. Here, we combine both features to fabricate the first solution-processed, monolithic, all-perovskite tandem and triple-junction solar cells.

David P. McMeekin, Suhas Mahesh, Nakita K. Noel, ..., Laura M. Herz, Michael B. Johnston, Henry J. Snaith

henry.snaith@physics.ox.ac.uk

HIGHLIGHTS

All-perovskite two-terminal tandem solar cells fabricated via solution processing

Acetonitrile/methylamine-based solvent can process narrow band-gap perovskite

Revealing the role of excess metal ions for mixed tin/lead perovskite systems

Proof of concept of the first monolithic all-perovskite triple-junction solar cell

McMeekin et al., Joule 3, 1–15
February 20, 2019
https://doi.org/10.1016/j.joule.2019.01.007

Please cite this article in press as: McMeekin et al., Solution-Processed All-Perovskite Multi-Junction Solar Cells, Joule (2019), https://doi.org/10.1016/j.joule.2019.01.007

Joule

CellPress

Article

Solution-Processed All-Perovskite Multi-Junction Solar Cells

David P. McMeekin,[1] Suhas Mahesh,[1] Nakita K. Noel,[1] Matthew T. Klug,[1] JongChul Lim,[1] Jonathan H. Warby,[1] James M. Ball,[1] Laura M. Herz,[1] Michael B. Johnston,[1] and Henry J. Snaith[1,2,*]

SUMMARY

Multi-junction device architectures can increase the power conversion efficiency (PCE) of photovoltaic (PV) cells beyond the single-junction thermodynamic limit. However, these devices are challenging to produce by solution-based methods, where dissolution of underlying layers is problematic. By employing a highly volatile acetonitrile(CH_3CN)/methylamine(CH_3NH_2) (ACN/MA) solvent-based perovskite solution, we demonstrate fully solution-processed absorber, transport, and recombination layers for monolithic all-perovskite tandem and triple-junction solar cells. By combining $FA_{0.83}Cs_{0.17}Pb(Br_{0.7}I_{0.3})_3$ (1.94 eV) and $MAPbI_3$ (1.57 eV) junctions, we reach two-terminal tandem PCEs of more than 15% (steady state). We show that a $MAPb_{0.75}Sn_{0.25}I_3$ (1.34 eV) narrow band-gap perovskite can be processed via the ACN/MA solvent-based system, demonstrating the first proof-of-concept, monolithic all-perovskite triple-junction solar cell with an open-circuit voltage reaching 2.83 V. Through optical and electronic modeling, we estimate the achievable PCE of a state-of-the-art triple-junction device architecture to be 26.7%. Our work opens new possibilities for large-scale, low-cost, printable perovskite multi-junction solar cells.

INTRODUCTION

Metal halide perovskite semiconductors exhibit high performance when integrated in optoelectronic devices such as light-emitting diodes (LEDs),[1] photo-detectors,[2,3] lasers,[4,5] and solar cells.[6–13] Perovskites have a general chemical formula, ABX_3, and allow their band gap to be tuned by substituting their chemical constituents, for example, the A-site cation can be methylammonium, formamidinium, or cesium (Cs), the B-site metal cation can be lead (Pb) or tin (Sn), and X-site anion can be iodide, bromide, or chloride, or more complex mixtures. This ease of ion substitution enables halide perovskite semiconductors to be tuned to absorb specific regions of the solar spectrum.[14,15]

Solar light is composed of a broad energy spectrum with significant intensity ranging from ultraviolet, with photon energies greater than 3 eV, to the infrared region with photon energies less than 1.7 eV to around 0.5 eV. When light is incident upon a semiconductor, light with energy greater than the band gap is absorbed, and the excess energy of the photons (above the band-gap energy) is lost as heat through thermalization of the electrons. Due to the thermalization process, the maximum voltage a photovoltaic (PV) cell can generate is always slightly less than the band-gap energy, and the maximum solar to electrical power conversion efficiency of a PV cell is obtained for a semiconductor with a band gap, which results in maximizing the product of voltage times current density. This has been calculated by Shockley and Queisser[16] and Tiedje-Yablonovitch,[17] who estimate the ideal band gap of a

Context & Scale

Silicon-based solar cells are dominating today's solar energy market. However, their efficiencies will soon reach their maximum practical limit. Without any gains in efficiency, price reductions will become increasingly difficult to achieve. Tandem and multi-junction architectures can overcome this single-junction efficiency limit. Perovskite materials offer both band-gap tunability and solution processability. This unique combination of properties allows for fabrication of multi-junction solar cells using high-throughput deposition techniques such as blade coating, roll-to-roll, gravure coating or inkjet printing. However, these solar cells have yet to be fabricated using these deposition techniques due to difficulties in sequentially depositing these semiconductors. By utilizing an acetonitrile/methylamine-based solvent, we demonstrate the first monolithic all-perovskite multi-junction solar cells fabricated via solution processing of all active layers, apart from the electrodes.

PV cell. Furthermore, this compromise between current and voltage places an absolute limit upon efficiency for PV cells composed of a single absorber layer to around 32.5%.[18] By reducing the difference between the photon energy and the electronic band-gap energy, we can effectively minimize charge-carrier thermalization losses. However, in order to capture a significant fraction of the sun light, multiple cells with different band gaps need to be stacked on top of each other, known as multi-junction cells. Through this approach, it is possible to raise the theoretical efficiency limit under 1 sun AM1.5 irradiance to 44.3% and 50.1% for double- and triple-junction cells, respectively.[19]

Recently, efficient solar cells employing wide band-gap perovskites have been fabricated by partial substitution of the organic A-site cation with Cs to improve their structural, thermal, and light stability.[20–30] Furthermore, narrow band-gap materials have also been explored through modifications to the B-site cation, where the partial substitution of Pb with Sn results in an anomalous band-gap bowing behavior, leading to band gaps approaching 1.2 eV.[31–39]

To date, perovskite solar cells exhibiting record efficiencies have been processed via solution-based fabrication methods, reaching 23.3% in a single-junction device.[40] The ability to fabricate high-quality absorber materials from solution-based processes has led to the rapid rise of perovskite solar cells.[6–13,41] In recent years, significant breakthroughs have been made in four-terminal (4T)[34,39,42–47] and two-terminal (2T)[24,39,48–53] perovskite-on-silicon,[42,43,46,49,51,54,55] perovskite-on-Cu(In,Ga)Se_2 (CIGS),[42,44,47,48,52] perovskite-on-$Cu_2ZnSn(S,Se)_4$ (CZTSSe),[48] and perovskite-on-perovskite[24,34,39,45,50,56–58] tandem cells. Moreover, Werner and al. recently fabricated the first perovskite/perovskite/silicon triple-junction solar cell in a step toward highly efficient photovoltaics.[59] Tandem solar cells require a semi-transparent electrode and/or recombination layers between each sub-cell. These highly conductive transparent layers have been fabricated using silver nanowires (Ag-NWs),[42] doped organic semiconductors such as N4,N4,N4,″N4″-tetra([1,1′-biphenyl]-4-yl)-[1,1′:4′,1″-terphenyl]-4,4″-diamine doped with 2,2′-(perfluoronaphthalene-2,6-diylidene) dimalononitrile (TaTm:F_6-TCNNQ),[50] poly(3,4-ethylenedioxythiophene) polystyrene sulfonate (PEDOT:PSS),[56,60] aluminum doped zinc oxide (AZO),[44] and, most notably, indium tin oxide (ITO).[24,34,45,48,49,53–55,61] These materials can also be processed using different deposition techniques such as: spray coating,[42] film transfer lamination,[60] vacuum deposition,[50] and sputter coating.[24,34,44,48,49,54,55,61] Sputtered ITO has gained considerable attention due to its high optical transparency throughout the visible and near-infrared (NIR) region, combined with a low resistivity.[62] Due to its dense and compact nature, this sputtered transparent conductive oxide (TCO) can also serve as a physical barrier to the solvents that are used to process the subsequent material layers, specifically, dimethyl formamide (DMF) and dimethyl sulfoxide (DMSO), both strongly coordinating solvents used in the dissolution of perovskite salts. These solvents rapidly re-dissolve any underlying perovskite layers unless they are protected by a dense pin-hole-free layer, such as ITO. Eperon, Leijtens, et al. showed that monolithic all-perovskite tandem cells can be fabricated using this dense, sputtered ITO layer.[39] Using this ITO interlayer, Zhao et al. recently fabricated an all-perovskite tandem reaching a power conversion efficiencies (PCEs) of 20.7%.[45] However, the re-dissolution problem has thus far prevented any experimental realization of a multi-junction perovskite solar cell being fabricated with all the active layers between the electrodes being solution processed.[39] These sputter-coated TCOs usually require high-vacuum deposition systems and additional buffer layers comprised of metal oxides deposited via atomic layer deposition (ALD), with the latter to prevent sputter damage of the organic and

[1]Clarendon Laboratory, Department of Physics, University of Oxford, Parks Road, Oxford OX1 3PU, UK

[2]Lead Contact

*Correspondence: henry.snaith@physics.ox.ac.uk

https://doi.org/10.1016/j.joule.2019.01.007

Please cite this article in press as: McMeekin et al., Solution-Processed All-Perovskite Multi-Junction Solar Cells, Joule (2019), https://doi.org/10.1016/j.joule.2019.01.007

perovskite layers. Furthermore, the lower refractive index of ITO, in comparison to the perovskite absorber layers, introduces significant internal reflective losses, thus limiting the maximum feasible power conversion efficiency.[63]

Herein, we employ an acetonitrile/methylamine (ACN/MA) composite solvent, which was previously introduced by Noel et al.,[64] to enable the sequential processing of perovskite absorber layers upon underlying perovskite devices. These fully solution-processed active, transport, and recombination layers for perovskite multi-junction architectures have the potential of being applied to the manufacturing of large-area films on both rigid and flexible substrates, using deposition techniques such as roll-to-roll (R2R) processing, blade coating, or inkjet printing. However, we note that additional work is required to solution-process both transparent and metal electrodes. Here, our solution-processed tandem architecture reaches over 15% steady-state PCE and delivers 2.18 V open-circuit voltage (V_{oc}). Furthermore, we show that the mixed-metal Sn/Pb perovskite $MAPb_{0.75}Sn_{0.25}I_3$ can also be processed via the ACN/MA solvent system, where the reducing nature of MA obviates the need to use SnF_2 to achieve respectable efficiencies, allowing us to obtain a scanned PCE of more than 11% (steady-state 10.5%), employing an n-i-p architecture. Using a mixed-metal $MAPb_{0.75}Sn_{0.25}I_3$ perovskite material to extend the light absorption of the multi-junction cell to 925 nm, we present the first all-perovskite, monolithic, triple-junction solar cell with a V_{oc} of 2.83 V. We utilize an optical and electronic model to validate our experimental results and reveal the optical losses existing within our specific experimental architecture. We then proceed to model a triple-junction perovskite solar cell, using electronic characteristics of currently feasible 1.94/1.57/1.24 eV perovskite materials, showing the possibility of achieving a triple-junction device with a 26.7% PCE and corresponding V_{oc} of 3.16 V.

RESULTS AND DISCUSSION

Due to charge conservation, the current density flowing out of each sub-cell in a multi-junction cell must match, and hence, the current will be limited by the lowest current density generated from any sub-cell. Thus, in order to maximize the photocurrent density in a 2T monolithic tandem, both sub-cells should generate equal current density, which can be achieved through carefully tuning the band gap and thickness of each junction. In the first instance, we develop a wide band-gap, Pb-based perovskite tandem cell by processing an ~1.94 eV (as determined by a Tauc plot which we show in Figure S1) front cell to complement a 1.57 eV rear cell. We process the wide band-gap junction first and hence do not have to overtly consider solvent orthogonality issues. We therefore follow a conventional solution-processing route and fabricate $FA_{0.83}Cs_{0.17}Pb(Br_{0.7}I_{0.3})_3$ with 2% (molarity with respect to the Pb) potassium (K^+) additive.[65–69] As we have previously described, we employed a deposition technique utilizing hydrohalic acidic as additives to fabricate highly ordered perovskite materials with grains reaching micron sizes in diameter (Figure S2).[70] Highly crystalline perovskite materials with low energetic disorder have been shown to suppress halide segregation.[71] Furthermore, as recent reports suggest,[60–66,70] we utilize potassium as an additive to suppress ionic migration and reduce the anomalous hysteretic behavior intrinsically present in perovskite solar cells.[72] For this absorber material, in single-junction perovskite solar cells, we obtain open-circuit voltages of up to 1.27 V and a steady-state power conversion efficiency of 10.9%, which we show in Figure S3. However, although our open-circuit voltages are higher compared to other ~1.75 eV materials,[20] we note that the voltage losses, with respect to the band-gap energy, are greater for this bromide-rich wide band-gap material. Hence, additional efforts are required to further increase V_{oc} and minimize non-radiative losses.

Please cite this article in press as: McMeekin et al., Solution-Processed All-Perovskite Multi-Junction Solar Cells, Joule (2019), https://doi.org/10.1016/j.joule.2019.01.007

All-perovskite monolithic 2T tandems and multi-junction solar cells require a tunnel junction (TJ) or recombination layer to provide a means to create an electronic series connection between the different sub-cells. Recombination layers between the sub-cells must fulfill stringent requirements. First, they must enable ohmic contact to the charge extraction layers and facilitate recombination of collected electrons and holes without introducing resistive losses. Second, they must be as optically transparent as possible to avoid parasitic absorption of light. Third, deposition of the recombination layer should not damage any of the layers beneath, which is typically achieved via introducing "buffer layers" when sputtering or by using orthogonal solvents for solution processing. Lastly, this interlayer must be a sufficient barrier to solvent penetration to prevent any re-dissolution of underlying perovskite or other electronic layers when subsequently processing another perovskite or charge extraction layer on top. Here, we introduce a recombination layer and an n-i-p perovskite solar cell architecture that meets these constraints. For the recombination layer, we find that a combination of a PEDOT:PSS followed by a ITO nanoparticles works well.

For the rear cell, which is processed on top of the wide-gap cell, we must consider the issue of dissolution of the underlying perovskite film. If we simply employ one of the standard DMF/DMSO solvent-based routes, we completely solvate and discolor the underlying perovskite film, even with our recombination layer present, making it evident that our recombination layer is not impermeable to DMF or DMSO (which we show in Video S1). We have previously developed an ACN/MA-based composite solvent system for processing perovskite films, which has several distinct advantages.[70] First, it is much more volatile than DMF, enabling very rapid drying. Second, the solvation strength can be tuned by varying the amount of methylamine incorporated. We chose the right amount of MA to enable complete dissolution of the salts but with minimal excess. We found that having an excess amount of MA in solution has a detrimental impact to the device. Unwanted pinholes in the interlayers may result in methylamine percolating and re-dissolving the perovskite underlayer. We find this solubility point by slowly adding an MA-saturated ACN/MA perovskite solution to a neat ACN perovskite dispersion, until the mixture becomes a clear perovskite solution.

To achieve optimal results, we found that careful tuning of the B-site metal ion content was needed for both $MAPbI_3$ and $MAPb_{0.75}Sn_{0.25}I_3$ perovskite material processed via the ACN/MA solvent route. Effects of non-stoichiometric perovskite precursor solutions have been regularly discussed;[73–77] however, the research community has yet to unanimously agree on which precise "non-stoichiometry" is ideal. Some studies have shown that excess organic ammonium lead to performance gains, while other studies showed the benefits of having excess PbI_2 in the precursor solution. However, it is clear that these small stoichiometric changes do impact the perovskite in various ways, such as effects on morphology,[74] luminescence,[75] trap passivation,[76] and stability.[77]

In Figure S4, we show a series of scanning electron microscope (SEM) top-view images of an $MAPbI_3$ perovskite film processed with the ACN/MA solvent system, with various non-stoichiometric compositions, ranging from 6% excess MAI to 6% excess PbI_2. We fabricated these films on top of the $FA_{0.83}Cs_{0.17}Pb(Br_{0.7}I_{0.3})_3$ front cell, including the PEDOT:PSS/ITO layer and a phenyl-C_{61}-butyric acid methyl ester ($PC_{61}BM$) electron extraction layer. We observed an impact on the morphology and surface coverage for precursor solutions with different compositions. In a solution-processed tandem architecture, it is imperative to eliminate the presence of

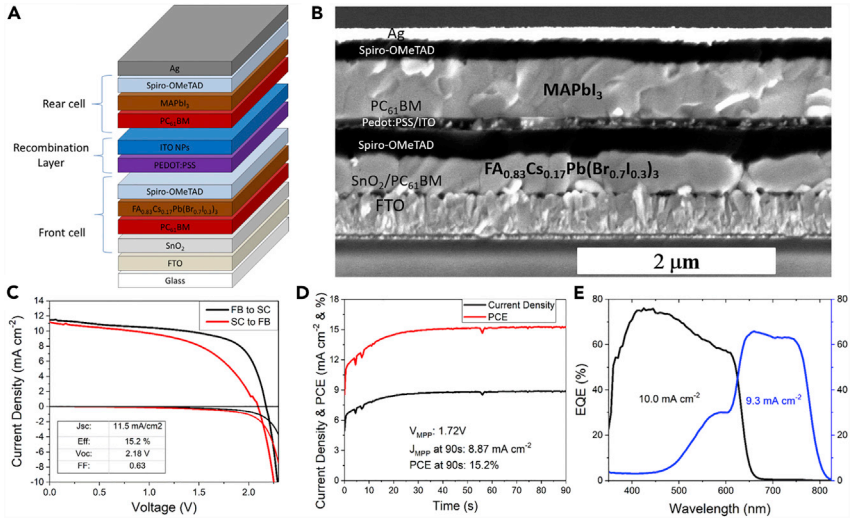

Figure 1. Two-Terminal $FA_{0.83}Cs_{0.17}Pb(Br_{0.7}I_{0.3})_3$/$MAPbI_3$ Tandem Perovskite Solar Cells

(A) Schematics showing an all-solution-processed perovskite/perovskite two-terminal (2T) tandem perovskite solar cell. Incoming light will be from below the device.

(B) SEM cross-section of the 2T perovskite/perovskite tandem.

(C) J-V characteristics for the champion $FA_{0.83}Cs_{0.17}Pb(Br_{0.7}I_{0.3})_3$/$MAPbI_3$ tandem heterojunction solar cell, with an equivalent irradiance of 104.25 mW cm^{-2}, measured at a 0.25 V/s scan rate. The active area of the solar cell is 0.0919 cm^{-2}.

(D) Photocurrent density and power conversion efficiency of champion $FA_{0.83}Cs_{0.17}Pb(Br_{0.7}I_{0.3})_3$/$MAPbI_3$ tandem heterojunction solar cell measured at the maximum power point for a 60 s time span.

(E) EQE spectrum for each sub-cell and the integrated current density for the tandem perovskite solar cell.

pinholes to prevent dissolution of underlying layers. In Figure S5, we show the tandem solar cell performance for devices processed with the differing range of compositions. We find that the ideal composition for maximizing the cell efficiency includes 3% excess MAI and proceed to optimize complete tandem solar cells with this composition. In Figures 1B and 1C, we show a schematic of a 2T tandem along with a corresponding SEM cross-section image. We fabricate the solar cells in the conventional n-i-p architecture and find that a recombination layer composed of PEDOT:PSS followed by ITO nanoparticles works remarkably well, sandwiched between a 2,2′,7,7′-tetrakis(N,N′-di-p-methoxyphenylamine)-9,9′-spirobifluorene (spiro-OMeTAD) p-type charge extraction layer and n-doped $PC_{61}BM$ electron transporter.

In Figure 1C, we show the forward and backward current-density voltage (J-V) characteristics of one of our highest-performing 2T tandem solar cells measured under a simulated air mass (AM) 1.5 solar irradiation with an equivalent mismatch corrected irradiance of 104.25 mW cm^{-2} upon the test cell. Our best tandem device generated a short-circuit current-density (J_{SC}) of 11.5 mA cm^{-2} (corrected to 11.0 mA cm^{-2} under 100 mW cm^{-2} AM1.5), a fill factor (FF) of 0.63, a V_{oc} of 2.18 V, giving a 15.22% J-V determined PCE, and a PCE of 15.20% under steady-state power output (SPO) conditions. In Figure 1D, we show the SPO, along with a histogram of performance parameters for a large batch of devices in Figure S6. We show in Figure 1E an external quantum efficiency (EQE) of both junctions, with an integrated current density of 10.0 mA cm^{-2} for the front cell and 9.3 mA cm^{-2} for the rear cell. During the EQE measurement, we applied a voltage bias to the solar cell equal to the V_{oc} of the

Please cite this article in press as: McMeekin et al., Solution-Processed All-Perovskite Multi-Junction Solar Cells, Joule (2019), https://doi.org/10.1016/j.joule.2019.01.007

optically biased sub-cell. This allowed for the EQE to be measured near J_{sc}. We note a moderate current-density mismatch between the two sub-cells. In Table S1, we show the calculated mismatch factor for each material used in the multi-junction solar cell. We note that the xenon arc lamp spectrum can be significantly different to the AM1.5G spectrum due to the large-intensity spikes in the infrared portion of the spectrum (shown in Figure S7). As a result, specific sub-cells of the multi-junction solar cell may be over or underestimated. In this specific case here, our tandem cell would be rear-cell limited under AM1.5G spectrum, but front-cell limited under the solar simulator lamp. To account for these discrepancies, we applied a mismatch factor correction with a KG5-filtered silicon reference cell, which reduced our estimated efficiency by a small factor of 1.004. The numbers we quote above are mismatch corrected. In the case of the triple junction, which we will discuss later on, a significant mismatch factor arises due to the xenon intensity spikes, which requires a reduction in efficiency by a factor of 1.486 to account for this mismatch factor when calibrating with a KG2-filtered silicon reference cell. As we show in Table S2, we have applied both correction factors to our reported efficiencies. Hence, in combination with our KG5 and KG2 Si reference cell measured at 103.83 mW cm^{-2} and 98.83 mW cm^{-2}, for the tandem and triple-junction solar cell, respectively, our equivalent AM1.5 irradiances are 104.25 mW cm^{-2} and 146.86 mW cm^{-2} for each solar cell architecture. We do note, however, that although we can accurately account for the spectral differences between the solar simulator and AM1.5 spectrum, we cannot accurately account for any change in fill factor, which may occur due to a difference between the sub-cell current mismatch under the different spectra. When the current between sub-cells in a tandem cell is mismatched, the FF is increased in comparison with the perfectly matched scenario. This positively compensates for current mismatch under real-world changing spectra but adds complications with efficiency estimations with single-zone solar simulators. For our tandem cell here, our sub-cells are more mismatched under true AM1.5 irradiance than under our simulator (due to the poor red response of our tandem cell and higher IR irradiance of our solar simulator). Therefore, if there is a significant impact from this effect, it would lead to a lower FF under our simulated light than under AM1.5 irradiance.

Estimation of voltage losses is a critical metric to access the quality of the recombination interlayers. As we show in Figure S8, using a PEDOT:PSS/ITO nanoparticle (NP) interlayer as the recombination layer, we measured a 2T tandem V_{oc} as high as 2.22 V, resulting in a interlayer voltage loss of approximately 160 mV, if we assume both sub-cells generated the highest measured single-junction V_{oc} of 1.27 V for the front cell and 1.11 V for the rear cell, under 1 sun illumination. However, we note that the rear cell will only be illuminated with half a sun in a tandem architecture, resulting in an ~18 mV loss in V_{oc} (assuming an ideality factor of 1), which reduces the losses attributed the interlayer to approximately 140 mV.

The long-term stability of our tandem architecture is a critical aspect that requires consideration. We note that the ACN/MA-based composite solvent system has been shown to readily dissolve methylammonium-based perovskites; however, due to poor salt solubility, more stable perovskites composed of FA and Cs mixed cation have yet to be fabricated using this solvent system. This inability to incorporate these ions may ultimately limit the attainable stability of our multi-junction solar cell. To address this issue, we have developed a post treatment, which incorporates FA^+, Cs^+, and Br^- ions into the $MAPbI_3$ crystal lattice while preserving a similar band gap and efficiency, which we show in Figure S9. This allows for partial substitution of the MA^+ and I^- ions with FA^+, Cs^+, and Br^- ions, forming an $(FA,MA,Cs)Pb(Br,I)_3$ material, thus enabling a pathway to stability using the ACN/MA solvent system.

Please cite this article in press as: McMeekin et al., Solution-Processed All-Perovskite Multi-Junction Solar Cells, Joule (2019), https://doi.org/10.1016/j.joule.2019.01.007

We show in Figure S10 that films of our mixed-cation Pb-mixed halide (FA,MA,Cs)$Pb(Br,I)_3$ material, processed from the MA/ACN solvent and post treatment, show much greater thermal stability than films of $MAPbI_3$ processed from the same solvent when stressed at 130°C in a nitrogen atmosphere.

Our recombination layer comprises PEDOT:PSS and ITO NP sublayers. We dilute a high-conductivity PEDOT:PSS (Heraus H1000) solution with isopropanol (IPA) and directly spin-coat upon the spiro-OMeTAD layer, which acts as both a recombination layer and a partial solvent barrier. We then spin-coat an ITO layer on top from a solvent dispersion of ITO NPs (>100 nm). The fabricated ITO NP layer may be porous and non-continuous. However, these NPs improve the recombination process, presumably due to their high carrier density, which allow holes from PEDOT:PSS and electrons from $PC_{61}BM$ to recombine. PEDOT:PSS is usually considered to be a material that may introduce instability into perovskite solar cells due to its hygroscopic nature.[78] In order test how stable our recombination layer is, we fabricated single-junction cells with the (FA,Cs)$Pb(Br,I)_3$ perovskite processed from a DMF solvent, with the addition of the complete recombination layer, including the PCBM electron transport layer, between the spiro-OMeTAD hole-transport layer and the gold electrode. We stressed the un-encapsulated devices at 85°C in an oven in an air atmosphere (ambient humidity ~50%) for more than 1,000 h and show the results in Figure S11. Unexpectedly, we observed an improvement in the thermal stability of the cells with the addition of our recombination layer, with the cells retaining over 70% of their initial performance after 1,000 h aging. This indicates that the added layers are not only relatively stable, but act as a partial encapsulant for the perovskite devices. However, we note that spiro-OMeTAD, along with its dopants, should ultimately be replaced with a more thermally stable hole-accepting layer to improve the overall stability of the device stack.

Although neat Pb-based devices have led to relatively stable perovskite materials, the drive to narrow the band gap using less stable Sn-based perovskites is still highly desirable for tandem applications.[79] As we show in Figure 2, we also studied the impact of non-stoichiometric precursor solutions on the material properties of the $MAPb_{0.75}Sn_{0.25}I_3$ perovskite (with a band gap of 1.34 eV determined from Tauc plots, Figure S12) by tuning the A-site to B-site ratio. In order to keep the intended $MAPb_{0.75}Sn_{0.25}I_3$ perovskite composition, we added excess PbI_2 and SnI_2 at a ratio of 75 to 25. In Figure 2A, we show Kelvin probe force microscopy (KPFM) images and observe a stark increase in work function as we incorporate excess metal ions in the $MAPb_{0.75}Sn_{0.25}I_3$ perovskite precursor solution. We also notice slower time-resolved photoluminescence (PL) decays, which we show in Figure 2B. In Figure 2C, we present the transient photo-conductivity for the corresponding samples for a range of excitation densities, measuring maximum perturbation of conductivity decay after photoexcitation by a 3.7 ns full-width half-maximum laser pulse.[80] Similarly, we observe an increase in early time photo-conductivity for films with excess metals ions, implying higher charge carrier mobility, or a small fraction of very rapid trapping on a shorter timescale than the laser pulse (sub few ns). We find that these longer-lived carrier lifetimes and higher photo-conductivities correlate to a substantial increase in device performance (Figure S13), which results in an optimized $MAPb_{0.75}Sn_{0.25}I_3$ PCE of more than 11%, as we show in Figure 2D.

Surprisingly, we found a substantial difference in optimum A-site to B-site ratio for Sn/Pb-based perovskite materials compared to neat Pb-based perovskites. In the case of Sn/Pb-based perovskite, the research community appears to have consistently observed performance gains when using an excess of Sn halides, most notably in the

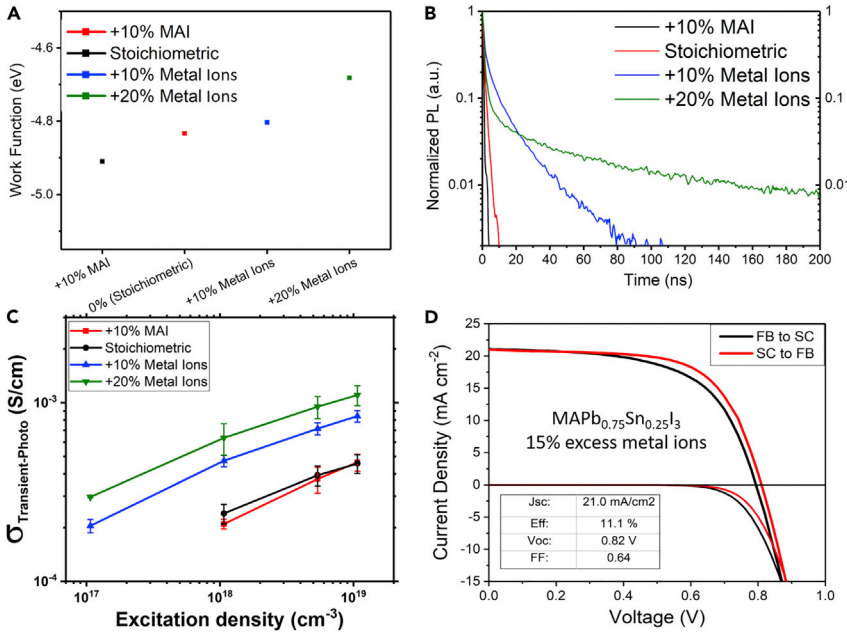

Figure 2. Impact of Varying the Composition of A- to B-Site Cations for ACN Processed $MAPb_{0.75}Sn_{0.25}I_3$ Perovskite Materials

(A) Kelvin-probe measurement of varying A- to B-site stoichiometry.

(B) Normalized time-resolved PL measurements taken at the peak emission wavelength of varying A- to B-site stoichiometry.

(C) Peak transient photoconductivity signal as a function of ns 470 nm laser pulse excitation density.

(D) J-V characteristics of an optimized $MAPb_{0.75}Sn_{0.25}I_3$ single-junction planar heterojunction solar cell with 15% excess metal ions, measured under 100.26 mW cm^{-2} equivalent AM1.5 irradiance at a 0.25 V/s scan rate. The masked aperture area of the solar cell is 0.0919 cm^{-2}.

form of tin fluoride (SnF_2)[45,81–84] or tin chloride ($SnCl_2$).[81] The tin fluoride as an additive has readily been used as a reducing agent with the aim of suppressing the tin oxidation from Sn^{2+} to Sn^{4+}. By suppressing oxidation, we limit Sn^{2+} vacancies, which causes the undesirable excessive p-type behavior found in Sn-based perovskites. In our study here, we rely on MA to act as a reducing agent instead of SnF_2,[85] since SnF_2 poorly dissolves in the ACN/MA solvent system. We show in Figure S13 a plot of non-optimized devices with various ratios of A-site to B-site cations. We find that devices with excess MAI produced near-zero PCE and little to no short-circuit density (J_{sc}), whereas devices with excess amounts of metals ions clearly show an increase in single-junction device efficiency, reaching an optimum composition with 15% excess metal ions. Thus, Sn-based perovskites not only require a reducing agent to suppress oxidation, but also require excess metal ions, which we assume act as "compensator" ions, to minimize the number of Sn vacancies. This is in agreement with the findings by Song et al., who observed that a non-stoichiometric $CsSnI_3$ perovskite composition of 0.4:1 of CsI:SnI_2 was required for optimum performance when processed under a reducing hydrazine atmosphere.[86] In Figure 2A, we notice a deeper Fermi level for the $MAPb_{0.75}Sn_{0.25}I_3$ perovskite with MAI-rich compositions, which is consistent with a higher concentration of Sn^{2+} vacancies, which are expected to lead to p-doping of the perovskite. In contrast, the shallower Fermi levels, which we observed for metal ion-rich perovskite films, would correspond to a more intrinsic perovskite material, indicative of fewer Sn^{2+} vacancies. We interpret the increase in carrier lifetimes in the perovskite absorber, which we observe in Figure 2A, to be consistent with and indicate a transition from a highly p-type material to a more intrinsic semiconductor.

Please cite this article in press as: McMeekin et al., Solution-Processed All-Perovskite Multi-Junction Solar Cells, Joule (2019), https://doi.org/10.1016/j.joule.2019.01.007

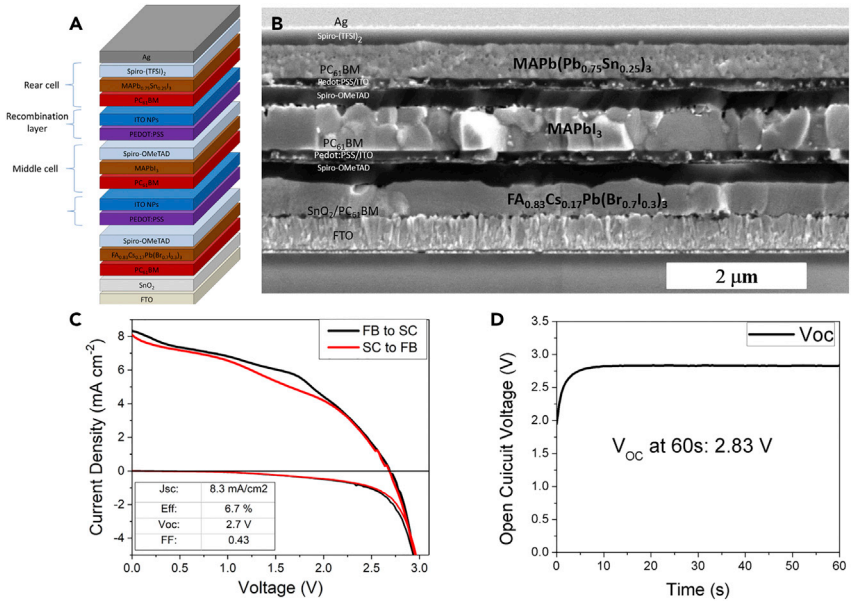

Figure 3. $FA_{0.83}Cs_{0.17}Pb(Br_{0.7}I_{0.3})_3/MAPbI_3/MAPb_{0.75}Sn_{0.25}I_3$ Triple-Junction Perovskite Solar Cells

(A) Schematics showing an all-solution-processed triple-junction two-terminal (2T) perovskite solar cell. Incoming light will be from bellow the device.

(B) SEM cross-section of the triple-junction 2T all-perovskite tandem. All the layers are labeled on the image.

(C) J-V characteristics for the champion $FA_{0.83}Cs_{0.17}Pb(Br_{0.7}I_{0.3})_3/MAPbI_3/MAPb_{0.75}Sn_{0.25}I_3$ triple-junction heterojunction solar cell fabricated, with an equivalent irradiance of 146.86 mW cm^{-2} measured at a 0.25 V/s scan rate. The active area of the solar cell is 0.0919 cm^{-2}.

(D) Steady-state open-circuit voltage (V_{oc}) of triple-junction planar heterojunction perovskite solar cell measured over a 60 s time span.

In Figure 3, we show the structure and performance characteristics of our all-perovskite, monolithic, triple-junction solar cell, prepared via solution processing. The narrow band-gap $MAPb_{0.75}Sn_{0.25}I_3$ perovskite solar cell, which we described in Figure 2, was processed on top of the dual-junction tandem solar cell architecture that we described in Figure 1. In Figure 3A, we show a schematic of the 2T triple-junction cell comprised of $FA_{0.83}Cs_{0.17}Pb(Br_{0.7}I_{0.3})_3/MAPbI_3/MAPb_{0.75}Sn_{0.25}I_3$. In Figure 3B, we show a corresponding SEM cross-section image. In Figure 3C, we show the forward and backward J-V characteristics of one of our highest-performing solar cells, measured under an equivalent irradiance of 146.86 mW cm^{-2}. We measured a J-V determined PCE of 6.7% (6.4% SPO, which we show in Figure S14). Our highest V_{oc}, which we show in Figure 3D, was measured on a separate device (shown in Figure S15) and exhibits a steady-state open-circuit voltage of 2.83 V after 60 s.

We note that the performance of the triple-junction is inferior to that of the double-junction solar cell due to the lower than anticipated short-circuit current-density generated by the $MAPb_{0.75}Sn_{0.25}I_3$ rear cell and the overall low FF. This low photo-generated current is responsible for severely current limiting the entire multi-junction cell. In Figure S16, we show a high-performing $FA_{0.83}Cs_{0.17}Pb_{0.5}Sn_{0.5}I_3$ perovskite in a p-i-n architecture, processed with a DMF/DMSO solvent, filtered with a $FA_{0.83}Cs_{0.17}Pb(Br_{0.7}I_{0.3})_3/MAPbI_3$ tandem solar cell without the Ag electrode. Although we note this is not a 4T tandem measurement since we did not employ a semi-transparent electrode upon the top tandem stack, this measurement allows us to roughly estimate the expected efficiency gain if

Please cite this article in press as: McMeekin et al., Solution-Processed All-Perovskite Multi-Junction Solar Cells, Joule (2019), https://doi.org/10.1016/j.joule.2019.01.007

higher performances and lower band gaps were obtained with ACN/MA solvent system route. As we show in Figure S16C, a junction based on $FA_{0.83}Cs_{0.17}Pb_{0.5}Sn_{0.5}I_3$ with a 1.22 eV absorption onset, 15.5% steady-state efficiency can be obtained when unfiltered and 2.4% steady-state efficiency when filtered with the $FA_{0.83}Cs_{0.17}Pb(Br_{0.7}I_{0.3})_3$/$MAPbI_3$ tandem. Thus, a narrow band-gap material could potentially boost the $FA_{0.83}Cs_{0.17}Pb(Br_{0.7}I_{0.3})_3$/$MAPbI_3$ by more than 2.4%, reaching 17.5% combined PCE. We also note that this measurement includes an air gap between the tandem cell and the narrow band-gap single-junction solar cell and an additional PEDOT:PSS layer that would otherwise not be present in the monolithic triple-junction solar cell. The EQE spectrum of the filtered cell, which we show in Figure S16B, clearly indicates significant panchromatic loss is photocurrent density beyond what we would expect simply from the parasitic absorbance is all the charge extraction and recombination layers, which we show in Figures S17 and S18. This loss is most likely due to the air gap and internal reflections between the stacked (non-monolithic) sub-cells.

As reported by Hörantner et al., all-perovskite triple-junction solar cells employing perovskite absorbers with similar band gaps to those that we have used in the present work should be capable of outperforming single- and double-junction efficiencies. The modeling of Hörantner et al. shows that an optimized 1.22 eV band-gap material should current match the two wider band-gap sub-cells of 2.04 eV and 1.58 eV, delivering a theoretical maximum J_{SC} of 12 mA cm^{-2}, a V_{oc} of 3.54 V and a PCE of 36.6%.[63] However, this performance can only be obtained with optically transparent interlayers to reduce parasitic absorption and reflection losses. In Figures S17 and S18, we show the optical properties of each interlayer that we have used in our multi-junction stack. We note that the ~60-nm-thick $PC_{61}BM$ layer that we employ is responsible for the majority of the parasitic absorption and reflection losses.

To understand in more detail where our present losses are arising and to assess the true potential of this solution-processed all-perovskite multi-junction solar cell architecture, we employed a similar optical and electrical model to that used by Hörantner et al. Using our experimental thicknesses, in combination with the extracted electrical characteristics of our best-performing single-junction perovskite cells of each band gap, we present in Figures 4A and 4B an estimation of the performance of our tandem stack and the corresponding modeled EQE spectrum. We estimate that our tandem solar cell (sub-cells with 1.94 eV and 1.57 eV band gaps) can be increased to nearly 19% by combining the electrical characteristics of our current measured champion $FA_{0.83}Cs_{0.17}Pb(Br_{0.7}I_{0.3})_3$ with our best-in-class ACN/MA $MAPbI_3$ device. We then proceed to model a stack with identical absorber and interlayer materials (shown in Figures 4C and 4D), but with a state-of-the-art $MAPbI_3$, processed via a DMF/DMSO route, an optimized perovskite thicknesses, interlayers with thickness down to 50 nm, and a MgF_2 anti-reflective coating. These improvements allow the tandem cell to reach a 21.8% PCE. In this figure, we also modeled an optimized stack with an enhanced front cell with improved electrical characteristics, assuming an electroluminescence efficiency (EQE_{EL}) of 1%, a series resistance (R_S) of $4 \cdot 10^{-2}\ \Omega\ cm^2$, and a shunt resistance (R_{SH}) of $10 M\Omega\ cm^2$ for the $FA_{0.83}Cs_{0.17}Pb(Br_{0.7}I_{0.3})_3$,[87] which increased the front cell PCE to 16.8% and the attainable tandem cell PCE to 26.8%. Figures 4E and 4F reveal the performance of our triple-junction architecture, assuming perovskite thicknesses optimized for current-matching with maximum thickness limited to 1,382 nm, state-of-art $MAPbI_3$ and $FA_{0.6}MA_{0.4}Pb_{0.4}Sn_{0.6}I_3$ perovskite sub-cells, and an anti-reflective coating is added on top. We can see that a 26.7% PCE can be achieved by using optimized thickness, and more than 30% PCE triple-junction efficiency is within reach by using

Please cite this article in press as: McMeekin et al., Solution-Processed All-Perovskite Multi-Junction Solar Cells, Joule (2019), https://doi.org/10.1016/j.joule.2019.01.007

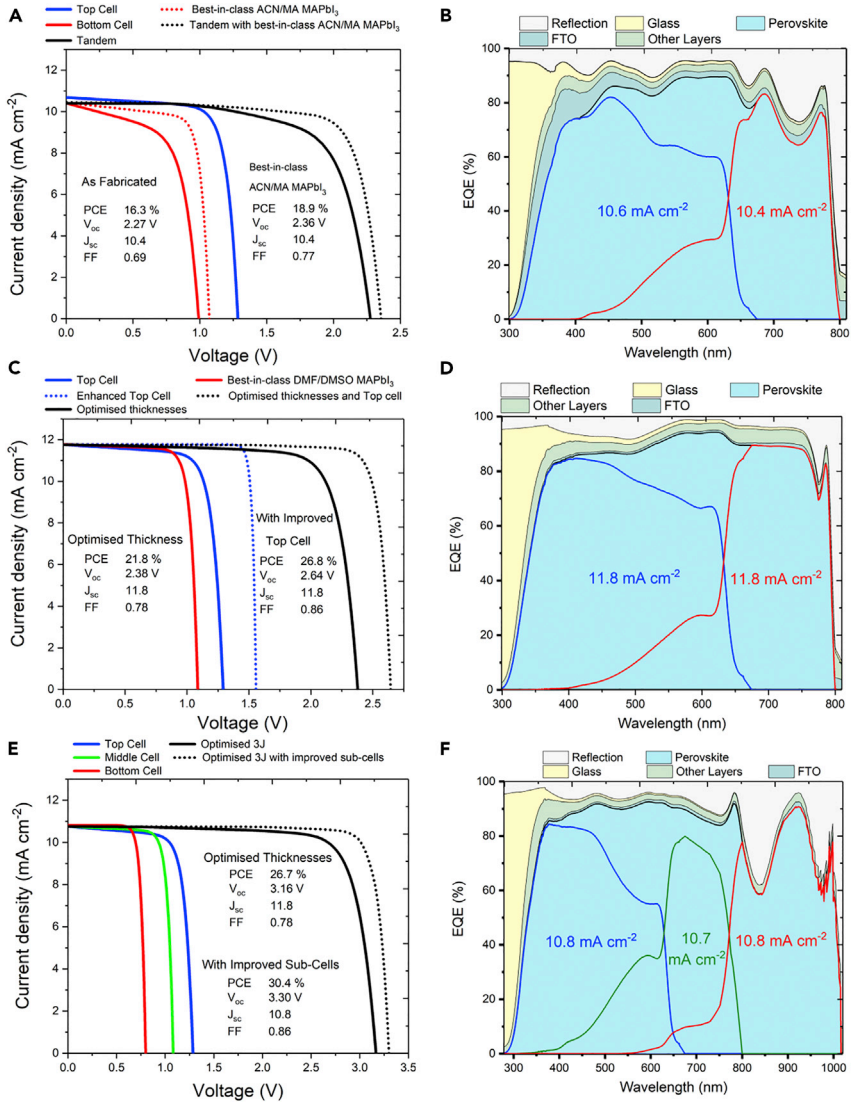

Figure 4. Optical and Electrical Modeling of Multi-Junction Perovskite Solar Cells

(A and B) Calculated J-V characteristics (A) and external quantum efficiency (EQE) (B) for the solution-processed $FA_{0.83}Cs_{0.17}Pb(Br_{0.7}I_{0.3})_3/MAPbI_3$ tandem solar cell, with current single-junction experimental data and with best-in-class ACN/MA $MAPbI_3$ single-junction cell.

(C and D) Calculated J-V characteristics (C) and EQE (D) of a $FA_{0.83}Cs_{0.17}Pb(Br_{0.7}I_{0.3})_3/MAPbI_3$ tandem solar cell, assuming optimized layers thicknesses, 50 nm interlayers, MgF_2 anti-reflection coating, and an enhanced TC performance.

(E and F) J-V characteristics (E) and EQE (F) for a $FA_{0.83}Cs_{0.17}Pb(Br_{0.7}I_{0.3})_3/MAPbI_3/FA_{0.6}MA_{0.4}Pb_{0.4}Sn_{0.6}I_3$ triple-junction architecture, assuming optimized layers thicknesses, 50 nm interlayers, MgF_2 anti-reflection coating, and an enhanced TC performance.

the enhanced front cell. We detail the specific layer thicknesses for each simulation, along with further details in the supplementary information.

To date, all-perovskite monolithic multi-junction solar cells have yet to surpass the efficiency of their state-of-the-art single-junction counterparts. The perovskite-on-silicon tandem cell is the only example yet realized that delivers greater efficiency than the world record for each sub-cell.[88] The perovskite junctions require significant improvements in light management to reduce reflection and parasitic absorption

losses. The most significant fundamental loss is the inability to generate a comparatively high V_{oc} from the wide band-gap cells. Furthermore, layer deposition uniformity has to be improved in order to realize charge extraction and recombination layers with thicknesses in the 50 nm range. However, with concerted effort, we expect these losses to be mitigated and hence enable fully solution-processed multi-junction cells to ultimately surpass state-of-the-art single-junction cell efficiencies.

EXPERIMENTAL PROCEDURES

Full details of experimental procedures can be found in the Supplemental Information.

SUPPLEMENTAL INFORMATION

Supplemental Information includes experimental procedures, 18 figures, two tables, and one video and can be found with this article online at https://doi.org/10.1016/j.joule.2019.01.007.

ACKNOWLEDGMENTS

This project was funded in part by EPSRC UK and the U.S. Office of Naval Research (ONR). The authors would like to acknowledge Dr. Severin N. Habisreutinger from the National Renewable Energy Laboratory for his valuable and enticing discussions on recombination layers comprised of carbon nanotubes.

AUTHOR CONTRIBUTIONS

D.P.M. and H.J.S. conceived the experiments. S.M. conducted the optical and electrical modeling of multi-junction perovskite. D.P.M., S.M., N.K.N., M.T.K., J.L., J.H.W., and J.M.B. conducted the experiments. D.P.M. wrote the original draft of the manuscript. H.J.S. supervised the project. L.M.H. and M.B.J. provided advice and expertise. All authors contributed to the final version of the manuscript.

DECLARATION OF INTERESTS

H.J.S. is a co-founder, Chief Scientific Officer, and a Director of Oxford PV Ltd. Oxford University have filed a patent related to the subject matter of this manuscript.

Received: October 14, 2018
Revised: December 3, 2018
Accepted: January 11, 2019
Published: January 18, 2019

REFERENCES

1. Sadhanala, A., Deschler, F., Thomas, T.H., Dutton, S.E., Goedel, K.C., Hanusch, F.C., Lai, M.L., Steiner, U., Bein, T., Docampo, P., et al. (2014). Preparation of single-phase films of CH3NH3Pb(I1-xBrx)3 with sharp optical band edges. J. Phys. Chem. Lett. *5*, 2501–2505.

2. Dou, L., Yang, Y.M., You, J., Hong, Z., Chang, W.H., Li, G., and Yang, Y. (2014). Solution-processed hybrid perovskite photodetectors with high detectivity. Nat. Commun. *5*, 5404.

3. Fang, Y., Dong, Q., Shao, Y., Yuan, Y., and Huang, J. (2015). Highly narrowband perovskite single-crystal photodetectors enabled by surface-charge recombination. Nat. Photonics *9*, 679–686.

4. Jia, Y., Kerner, R.A., Grede, A.J., Rand, B.P., and Giebink, N.C. (2017). Continuous-wave lasing in an organic–inorganic lead halide perovskite semiconductor. Nat. Photonics *11*, 784–788.

5. Zhu, H., Fu, Y., Meng, F., Wu, X., Gong, Z., Ding, Q., Gustafsson, M.V., Trinh, M.T., Jin, S., and Zhu, X.Y. (2015). Lead halide perovskite nanowire lasers with low lasing thresholds and high quality factors. Nat. Mater. *14*, 636–642.

6. Kojima, A., Teshima, K., Shirai, Y., and Miyasaka, T. (2009). Organometal halide perovskites as visible-light sensitizers for photovoltaic cells. J. Am. Chem. Soc. *131*, 6050–6051.

7. Lee, M.M., Teuscher, J., Miyasaka, T., Murakami, T.N., and Snaith, H.J. (2012). Efficient hybrid solar cells based on meso-superstructured organometal halide perovskites. Science *338*, 643–647.

8. Liu, M., Johnston, M.B., and Snaith, H.J. (2013). Efficient planar heterojunction perovskite solar cells by vapour deposition. Nature *501*, 395–398.

9. Burschka, J., Pellet, N., Moon, S.-J., Humphry-Baker, R., Gao, P., Nazeeruddin, M.K., and Grätzel, M. (2013). Sequential deposition as a route to high-performance perovskite-sensitized solar cells. Nature *499*, 316–319.

10. Malinkiewicz, O., Yella, A., Lee, Y.H., Espallargas, G.M., Graetzel, M., Nazeeruddin, M.K., et al. (2013). Perovskite solar cells employing organic charge-transport layers. Nat. Photonics *8*, 128–132.

11. Stranks, S.D., Eperon, G.E., Grancini, G., Menelaou, C., Alcocer, M.J.P., Leijtens, T., Herz, L.M., Petrozza, A., and Snaith, H.J. (2013). Electron-hole diffusion lengths exceeding 1 micrometer in an organometal trihalide perovskite absorber. Science *342*, 341–344.

12. Kim, H.S., Lee, C.R., Im, J.H., Lee, K.B., Moehl, T., Marchioro, A., Moon, S.J., Humphry-Baker, R., Yum, J.H., Moser, J.E., et al. (2012). Lead iodide perovskite sensitized all-solid-state submicron thin film mesoscopic solar cell with efficiency exceeding 9%. Sci. Rep. *2*, 591.

13. Im, J.-H., Lee, C.-R., Lee, J.-W., Park, S.-W., and Park, N.-G. (2011). 6.5% efficient perovskite quantum-dot-sensitized solar cell. Nanoscale *3*, 4088–4093.

14. Eperon, G.E., Stranks, S.D., Menelaou, C., Johnston, M.B., Herz, L.M., and Snaith, H.J. (2014). Formamidinium lead trihalide: a broadly tunable perovskite for efficient planar heterojunction solar cells. Energy Environ. Sci. *7*, 982–988.

15. Noh, J.H., Im, S.H., Heo, J.H., Mandal, T.N., and Seok, S.I. (2013). Chemical management for colorful, efficient, and stable inorganic-organic hybrid nanostructured solar cells. Nano Lett. *13*, 1764–1769.

16. Shockley, W., and Queisser, H.J. (1961). Detailed balance limit of efficiency of *p-n* junction solar cells. J. Appl. Physiol. *32*, 510–519.

17. Tiedje, T., Yablonovitch, E., Cody, G.D., and Brooks, B.G. (1984). Limiting efficiency of silicon solar cells. IEEE Trans. Electron Dev. *31*, 711–716.

18. Hirst, L.C., and Ekins-Daukes, N.J. (2011). Fundamental losses in solar cells. Prog. Photovolt. *19*, 286–293.

19. Araújo, G.L., and Martí, A. (1994). Absolute limiting efficiencies for photovoltaic energy conversion. Sol. Energy Mater. Sol. Cells *33*, 213–240.

20. McMeekin, D.P., Sadoughi, G., Rehman, W., Eperon, G.E., Saliba, M., Hörantner, M.T., Haghighirad, A., Sakai, N., Korte, L., Rech, B., et al. (2016). A mixed-cation lead mixed-halide perovskite absorber for tandem solar cells. Science *351*, 151–155.

21. Beal, R.E., Slotcavage, D.J., Leijtens, T., Bowring, A.R., Belisle, R.A., Nguyen, W.H., Burkhard, G.F., Hoke, E.T., and McGehee, M.D. (2016). Cesium lead halide perovskites with improved stability for tandem solar cells. J. Phys. Chem. Lett. *7*, 746–751.

22. Li, Z., Yang, M., Park, J.-S., Wei, S.-H., Berry, J.J., and Zhu, K. (2016). Stabilizing perovskite structures by tuning tolerance factor: formation of formamidinium and cesium lead iodide solid-state alloys. Chem. Mater. *28*, 284–292.

23. Sutton, R.J., Eperon, G.E., Miranda, L., Parrott, E.S., Kamino, B.A., Patel, J.B., et al. (2016). Bandgap-tunable cesium lead halide perovskites with high thermal stability for efficient solar cells. Adv. Energy Mater. https://doi.org/10.1002/aenm.201502458.

24. Rajagopal, A., Yang, Z., Jo, S.B., Braly, I.L., Liang, P.-W., Hillhouse, H.W., and Jen, A.K. (2017). Highly efficient perovskite-perovskite tandem solar cells reaching 80% of the theoretical limit in photovoltage. Adv. Mater. *29*, 1702140.

25. Chen, S., Hou, Y., Chen, H., Tang, X., Langner, S., Li, N., et al. (2017). Exploring the stability of novel wide bandgap perovskites by a robot based high throughput approach. Adv. Energy Mater.

26. Saliba, M., Matsui, T., Seo, J.-Y., Domanski, K., Correa-Baena, J.-P., Nazeeruddin, M.K., Zakeeruddin, S.M., Tress, W., Abate, A., Hagfeldt, A., and Grätzel, M. (2016). Cesium-containing triple cation perovskite solar cells: improved stability, reproducibility and high efficiency. Energy Environ. Sci. *9*, 1989–1997.

27. Wang, Z., Lin, Q., Chmiel, F.P., Sakai, N., Herz, L.M., and Snaith, H.J. (2017). Efficient ambient-air-stable solar cells with 2D-3D hetero-structured butylammonium-caesium-formamidinium lead halide perovskites. Nat. Energy *2*, 17135.

28. Lee, J.-W., Kim, D.-H., Kim, H.-S., Seo, S.-W., Cho, S.M., and Park, N.-G. (2015). Formamidinium and cesium hybridization for photo- and moisture-stable perovskite solar cell. Adv. Energy Mater. *5*, 1501310.

29. Yi, C., Luo, J., Meloni, S., Boziki, A., Ashari-Astani, N., Grätzel, C., et al. (2015). Entropic stabilization of mixed A-cation ABX_3 metal halide perovskites for high performance perovskite solar cells. Energy Environ. Sci. *9*, 656–662.

30. Kulbak, M., Gupta, S., Kedem, N., Levine, I., Bendikov, T., Hodes, G., and Cahen, D. (2016). Cesium enhances long-term stability of lead bromide perovskite-based solar cells. J. Phys. Chem. Lett. *7*, 167–172.

31. Stoumpos, C.C., Malliakas, C.D., and Kanatzidis, M.G. (2013). Semiconducting tin and lead iodide perovskites with organic cations: phase transitions, high mobilities, and near-infrared photoluminescent properties. Inorg. Chem. *52*, 9019–9038.

32. Noel, N.K., Stranks, S.D., Abate, A., Wehrenfennig, C., Guarnera, S., Haghighirad, A.-A., et al. (2014). Lead-free organic–inorganic tin halide perovskites for photovoltaic applications. Energy Environ. Sci. *7*, 3061–3068.

33. Hao, F., Stoumpos, C.C., Chang, R.P.H., and Kanatzidis, M.G. (2014). Anomalous band gap behavior in mixed Sn and Pb perovskites enables broadening of absorption spectrum in solar cells. J. Am. Chem. Soc. *136*, 8094–8099.

34. Yang, Z., Rajagopal, A., Chueh, C.-C., Jo, S.B., Liu, B., Zhao, T., and Jen, A.K. (2016). Stable low-bandgap Pb-Sn binary perovskites for tandem solar cells. Adv. Mater. *28*, 8990–8997.

35. Rajagopal, A., Liang, P.-W., Chueh, C.-C., Yang, Z., and Jen, A.K.-Y. (2017). Defect passivation via a graded fullerene heterojunction in low-bandgap Pb–Sn binary perovskite photovoltaics. ACS Energy Lett. *2*, 2531–2539.

36. Li, L., Zhang, F., Hao, Y., Sun, Q., Li, Z., Wang, H., et al. (2017). High efficiency planar Sn–Pb binary perovskite solar cells: controlled growth of large grains via a one-step solution fabrication process. J. Mater. Chem. C Mater. Opt. Electron. Devices *5*, 2360–2367.

37. Lee, S., and Kang, D.-W. (2017). Highly efficient and stable Sn-rich perovskite solar cells by introducing bromine. ACS Appl. Mater. Interfaces *9*, 22432–22439.

38. Liao, W., Zhao, D., Yu, Y., Shrestha, N., Ghimire, K., Grice, C.R., Wang, C., Xiao, Y., Cimaroli, A.J., Ellingson, R.J., et al. (2016). Fabrication of efficient low-bandgap perovskite solar cells by combining formamidinium tin iodide with methylammonium lead iodide. J. Am. Chem. Soc. *138*, 12360–12363.

39. Eperon, G.E., Leijtens, T., Bush, K.A., Prasanna, R., Green, T., Wang, J.T.-W., McMeekin, D.P., Volonakis, G., Milot, R.L., May, R., et al. (2016). Perovskite-perovskite tandem photovoltaics with optimized band gaps. Science *354*, 861–865.

40. NREL (2018). Best Research-Cell Efficiencies. https://www.nrel.gov/pv/assets/images/efficiency-chart-20180716.jpg.

41. Kagan, C.R., Mitzi, D.B., and Dimitrakopoulos, C.D. (1999). Organic-inorganic hybrid materials as semiconducting channels in thin-film field-effect transistors. Science *286*, 945–947.

42. Bailie, C.D., Christoforo, M.G., Mailoa, J.P., Bowring, A.R., Unger, E.L., Nguyen, W.H., et al. (2015). Semi-transparent perovskite solar cells for tandems with silicon and CIGS. Energy Environ. Sci. *8*, 956–963.

43. Werner, J., Barraud, L., Walter, A., Bräuninger, M., Sahli, F., Sacchetto, D., et al. (2016). Efficient near-infrared-transparent perovskite solar cells enabling direct comparison of 4-terminal and monolithic perovskite/silicon tandem cells. ACS Energy Lett. *1*, 474–480.

44. Pisoni, S., Fu, F., Feurer, T., Makha, M., Bissig, B., Nishiwaki, S., et al. (2017). Flexible NIR-transparent perovskite solar cells for all-thin-film tandem photovoltaic devices. J. Mater. Chem. A Mater. Energy Sustain. *5*, 13639–13647.

45. Zhao, D., Yu, Y., Wang, C., Liao, W., Shrestha, N., Grice, C.R., et al. (2017). Low-bandgap mixed tin–lead iodide perovskite absorbers with long carrier lifetimes for all-perovskite tandem solar cells. Nat. Energy *2*, 17018.

46. Duong, T., Wu, Y., Shen, H., Peng, J., Fu, X., Jacobs, D., et al. (2017). Rubidium multication perovskite with optimized bandgap for perovskite-silicon tandem with over 26% efficiency. Adv. Energy Mater. *7*, 1700228.

47. Shen, H., Duong, T., Peng, J., Jacobs, D., Wu, N., Gong, J., et al. (2018). Mechanically-stacked perovskite/CIGS tandem solar cells with efficiency of 23.9% and reduced oxygen sensitivity. Energy Environ. Sci. *11*, 394–406.

48. Todorov, T., Gershon, T., Gunawan, O., Sturdevant, C., and Guha, S. (2014). Perovskite-kesterite monolithic tandem solar cells with high open-circuit voltage. Appl. Phys. Lett. *105*, 173902.

49. Werner, J., Weng, C.-H., Walter, A., Fesquet, L., Seif, J.P., De Wolf, S., Niesen, B., and Ballif, C.

(2016). Efficient monolithic perovskite/silicon tandem solar cell with cell area >1 cm(2). J. Phys. Chem. Lett. *7*, 161–166.

50. Forgács, D., Gil-Escrig, L., Pérez-Del-Rey, D., Momblona, C., Werner, J., Niesen, B., et al. (2017). Efficient monolithic perovskite/perovskite tandem solar cells. Adv. Energy Mater. *7*, 1602121.

51. Sahli, F., Werner, J., Kamino, B.A., Bräuninger, M., Monnard, R., Paviet-Salomon, B., Barraud, L., Ding, L., Diaz Leon, J.J., Sacchetto, D., et al. (2018). Fully textured monolithic perovskite/silicon tandem solar cells with 25.2% power conversion efficiency. Nat. Mater. *17*, 820–826.

52. Han, Q., Hsieh, Y.-T., Meng, L., Wu, J.-L., Sun, P., Yao, E.-P., Chang, S.Y., Bae, S.H., Kato, T., Bermudez, V., and Yang, Y. (2018). High-performance perovskite/Cu(In,Ga)Se_2 monolithic tandem solar cells. Science *361*, 904–908.

53. Zhao, D., Chen, C., Wang, C., Junda, M.M., Song, Z., Grice, C.R., et al. (2018). Efficient two-terminal all-perovskite tandem solar cells enabled by high-quality low-bandgap absorber layers. Nat. Energy *1*, https://doi.org/10.1038/s41560-018-0278-x.

54. Bush, K.A., Palmstrom, A.F., Yu, Z.J., Boccard, M., Cheacharoen, R., Mailoa, J.P., et al. (2017). 23.6%-efficient monolithic perovskite/silicon tandem solar cells with improved stability. Nat. Energy *2*, 17009.

55. Albrecht, S., Saliba, M., Correa Baena, J.P., Lang, F., Kegelmann, L., Mews, M., et al. (2016). Monolithic perovskite/silicon-heterojunction tandem solar cells processed at low temperature. Energy Environ. Sci. *9*, 81–88.

56. Sheng, R., Hoerantner, M.T., Wang, Z., Jiang, Y., Zhang, W., Agosti, A., et al. (2017). Monolithic wide band gap perovskite/perovskite tandem solar cells with organic recombination layers. J. Phys. Chem. C *121*, 27256–27262.

57. Zhao, D., Wang, C., Song, Z., Yu, Y., Chen, C., Zhao, X., et al. (2018). Four-terminal all-perovskite tandem solar cells achieving power conversion efficiencies exceeding 23%. ACS Energy Lett *305–6*, https://doi.org/10.1021/acsenergylett.7b01287.

58. Ávila, J., Momblona, C., Boix, P., Sessolo, M., Anaya, M., Lozano, G., et al. (2018). High voltage vacuum-deposited $CH_3NH_3PbI_3$–$CH_3NH_3PbI_3$ tandem solar cells. Energy Environ. Sci. *11*, 3292–3297.

59. Werner, J., Sahli, F., Fu, F., Diaz Leon, J.J., Walter, A., Kamino, B.A., et al. (2018). Perovskite/perovskite/silicon monolithic triple-junction solar cells with a fully textured design. ACS Energy Lett *3*, 2052–2058.

60. Jiang, F., Liu, T., Luo, B., Tong, J., Qin, F., Xiong, S., et al. (2016). A two-terminal perovskite/perovskite tandem solar cell. J. Mater. Chem. A Mater. Energy Sustain. *4*, 1208–1213.

61. Wu, Y., Yan, D., Peng, J., Duong, T., Wan, Y., Phang, S.P., et al. (2017). Monolithic perovskite/silicon-homojunction tandem solar cell with over 22% efficiency. Energy Environ. Sci. *10*, 2472–2479.

62. Ellmer, K. (2012). Past achievements and future challenges in the development of optically transparent electrodes. Nat. Photonics *6*, 809–817.

63. Hörantner, M.T., Leijtens, T., Ziffer, M.E., Eperon, G.E., Christoforo, M.G., McGehee, M.D., et al. (2017). The potential of multijunction perovskite solar cells. ACS Energy Lett. *2*, 2506–2513.

64. Noel, N.K., Habisreutinger, S.N., Wenger, B., Klug, M.T., Hörantner, M.T., Johnston, M.B., et al. (2017). A low viscosity, low boiling point, clean solvent system for the rapid crystallisation of highly specular perovskite films. Energy Environ. Sci. *10*, 145–152.

65. Tang, Z., Bessho, T., Awai, F., Kinoshita, T., Maitani, M.M., Jono, R., Murakami, T.N., Wang, H., Kubo, T., Uchida, S., and Segawa, H. (2017). Hysteresis-free perovskite solar cells made of potassium-doped organometal halide perovskite. Sci. Rep. *7*, 12183.

66. Nam, J.K., Chai, S.U., Cha, W., Choi, Y.J., Kim, W., Jung, M.S., Kwon, J., Kim, D., and Park, J.H. (2017). Potassium incorporation for enhanced performance and stability of fully inorganic cesium lead halide perovskite solar cells. Nano Lett. *17*, 2028–2033.

67. uz Zaman, M.M., Imran, M., Saleem, A., Kamboh, A.H., Arshad, M., Khan, N.A., and Akhter, P. (2017). Potassium doped methylammonium lead iodide (MAPbI3) thin films as a potential absorber for perovskite solar cells; structural, morphological, electronic and optoelectric properties. Phys. B Condens. Matter. *522*, 57–65.

68. Bu, T., Liu, X., Zhou, Y., Yi, J., Huang, X., Luo, L., et al. (2017). A novel quadruple-cation absorber for universal hysteresis elimination for high efficiency and stable perovskite solar cells. Energy Environ. Sci. *10*, 2509–2515.

69. Abdi-Jalebi, M., Andaji-Garmaroudi, Z., Cacovich, S., Stavrakas, C., Philippe, B., Richter, J.M., Alsari, M., Booker, E.P., Hutter, E.M., Pearson, A.J., et al. (2018). Maximizing and stabilizing luminescence from halide perovskites with potassium passivation. Nature *555*, 497–501.

70. McMeekin, D.P., Wang, Z., Rehman, W., Pulvirenti, F., Patel, J.B., Noel, N.K., Johnston, M.B., Marder, S.R., Herz, L.M., and Snaith, H.J. (2017). Crystallization kinetics and morphology control of formamidinium-cesium mixed-cation lead mixed-halide perovskite via tunability of the colloidal precursor solution. Adv. Mater. *29*, https://doi.org/10.1002/adma.201607039.

71. Rehman, W., Milot, R.L., Eperon, G.E., Wehrenfennig, C., Boland, J.L., Snaith, H.J., Johnston, M.B., and Herz, L.M. (2015). Charge-carrier dynamics and mobilities in formamidinium lead mixed-halide perovskites. Adv. Mater. *27*, 7938–7944.

72. Snaith, H.J., Abate, A., Ball, J.M., Eperon, G.E., Leijtens, T., Noel, N.K., Stranks, S.D., Wang, J.T., Wojciechowski, K., and Zhang, W. (2014). Anomalous hysteresis in perovskite solar cells. J. Phys. Chem. Lett. *5*, 1511–1515.

73. Roldán-Carmona, C., Gratia, P., Zimmermann, I., Grancini, G., Gao, P., Graetzel, M., et al. (2015). High efficiency methylammonium lead triiodide perovskite solar cells: the relevance of non-stoichiometric precursors. Energy Environ. Sci. *8*, 3550–3556.

74. Yang, M., Li, Z., Reese, M.O., Reid, O.G., Kim, D.H., Siol, S., et al. (2017). Perovskite ink with wide processing window for scalable high-efficiency solar cells. Nat. Energy *2*, 17038, https://doi.org/10.1038/nenergy.2017.38.

75. Bi, D., Tress, W., Dar, M.I., Gao, P., Luo, J., Renevier, C., Schenk, K., Abate, A., Giordano, F., Correa Baena, J.P., et al. (2016). Efficient luminescent solar cells based on tailored mixed-cation perovskites. Sci. Adv. *2*, e1501170.

76. Chen, Q., Zhou, H., Song, T.-B., Luo, S., Hong, Z., Duan, H.-S., Dou, L., Liu, Y., and Yang, Y. (2014). Controllable self-induced passivation of hybrid lead iodide perovskites toward high performance solar cells. Nano Lett. *14*, 4158–4163.

77. Jacobsson, T.J., Correa-Baena, J.-P., Halvani Anaraki, E., Philippe, B., Stranks, S.D., Bouduban, M.E.F., Tress, W., Schenk, K., Teuscher, J., Moser, J.E., et al. (2016). Unreacted PbI_2 as a double-edged sword for enhancing the performance of perovskite solar cells. J. Am. Chem. Soc. *138*, 10331–10343.

78. Liu, J., Pathak, S.K., Sakai, N., Sheng, R., Bai, S., Wang, Z., et al. (2016). Identification and mitigation of a critical interfacial instability in perovskite solar cells employing copper thiocyanate hole-transporter. Adv. Mater. Interfaces *3*, 1600571.

79. Eperon, G.E., Hörantner, M.T., and Snaith, H.J. (2017). Metal halide perovskite tandem and multiple-junction photovoltaics. Nat. Rev. Chem. https://doi.org/10.1038/s41570-017-0095.

80. Leijtens, T., Lim, J., Teuscher, J., Park, T., and Snaith, H.J. (2013). Charge density dependent mobility of organic hole-transporters and mesoporous TiO_2 determined by transient mobility spectroscopy: implications to dye-sensitized and organic solar cells. Adv. Mater. *25*, 3227–3233.

81. Marshall, K.P., Walker, M., Walton, R.I., and Hatton, R.A. (2016). Enhanced stability and efficiency in hole-transport-layer-free CsSnI3 perovskite photovoltaics. Nat. Energy *1*, 16178.

82. Lee, S.J., Shin, S.S., Kim, Y.C., Kim, D., Ahn, T.K., Noh, J.H., Seo, J., and Seok, S.I. (2016). Fabrication of efficient formamidinium tin iodide perovskite solar cells through SnF_2-Pyrazine complex. J. Am. Chem. Soc. *138*, 3974–3977.

83. Kumar, M.H., Dharani, S., Leong, W.L., Boix, P.P., Prabhakar, R.R., Baikie, T., Shi, C., Ding, H., Ramesh, R., Asta, M., et al. (2014). Lead-free halide perovskite solar cells with high photocurrents realized through vacancy modulation. Adv. Mater. *26*, 7122–7127.

84. Kontos, A.G., Kaltzoglou, A., Siranidi, E., Palles, D., Angeli, G.K., Arfanis, M.K., Psycharis, V., Raptis, Y.S., Kamitsos, E.I., Trikalitis, P.N., et al. (2017). Structural stability, vibrational properties, and photoluminescence in $CsSnI_3$ perovskite upon the addition of SnF_2. Inorg. Chem. *56*, 84–91.

85. Newman, J.D., and Blanchard, G.J. (2006). Formation of gold nanoparticles using amine reducing agents. Langmuir *22*, 5882–5887.

86. Song, T.-B., Yokoyama, T., Aramaki, S., and Kanatzidis, M.G. (2017). Performance enhancement of lead-free tin-based perovskite solar cells with reducing atmosphere-assisted dispersible additive. ACS Energy Lett *2*, 897–903.

87. Hörantner, M.T., and Snaith, H.J. (2017). Predicting and optimising the energy yield of perovskite-on-silicon tandem solar cells under real world conditions. Energy Environ. Sci. *10*, 1983–1993.

88. Oxford, P.V. (2018). Oxford PV sets world record for perovskite solar cell. https://www.oxfordpv.com/news/oxford-pv-sets-world-record-perovskite-solar-cell.

JOUL, Volume *3*

Supplemental Information

Solution-Processed All-Perovskite Multi-Junction Solar Cells

David P. McMeekin, Suhas Mahesh, Nakita K. Noel, Matthew T. Klug, JongChul Lim, Jonathan H. Warby, James M. Ball, Laura M. Herz, Michael B. Johnston, and Henry J. Snaith

Joule

CellPress

Article Type

Solution-Processed All-Perovskite Multi-Junction Solar Cells

David P. McMeekin,[1] Suhas Mahesh,[1] Nakita K. Noel,[1] Matthew T. Klug,[1] JongChul Lim,[1] Jonathan H. Warby,[1] James M. Ball,[1] Laura M. Herz,[1] Michael B. Johnston,[1] and Henry J. Snaith[1,2]*

[1]Clarendon Laboratory, Department of Physics, University of Oxford, Parks Road, Oxford, OX1 3PU, UK

[2]Lead Contact

*Correspondence: henry.snaith@physics.ox.ac.uk

SUPPLEMENTARY INFORMATION

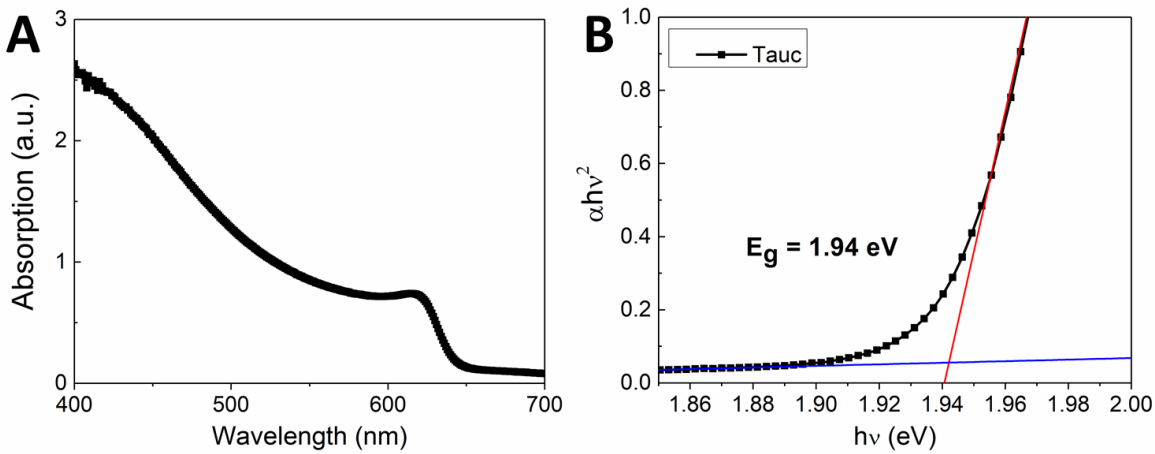

Figure S1 Optical characterization of $FA_{0.83}Cs_{0.17}Pb(Br_{0.7}I_{0.3})_3$ perovskite material with 2% potassium additive A) Absorption spectrum of $FA_{0.83}Cs_{0.17}Pb(Br_{0.7}I_{0.3})_3$ measured with an integration sphere. B) Tauc plot of **$FA_{0.83}Cs_{0.17}Pb(Br_{0.7}I_{0.3})_3$** perovskite assuming direct band gap material and fitting of optical band gap from intercept.

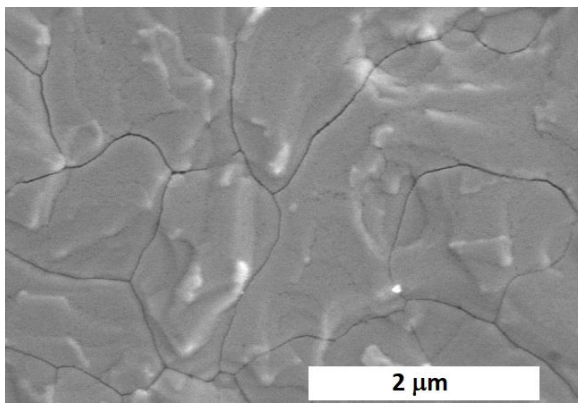

Figure S2 Scanning electron microscopy (SEM) image of the top view of $FA_{0.83}Cs_{0.17}Pb(Br_{0.7}I_{0.3})_3$ perovskite film.

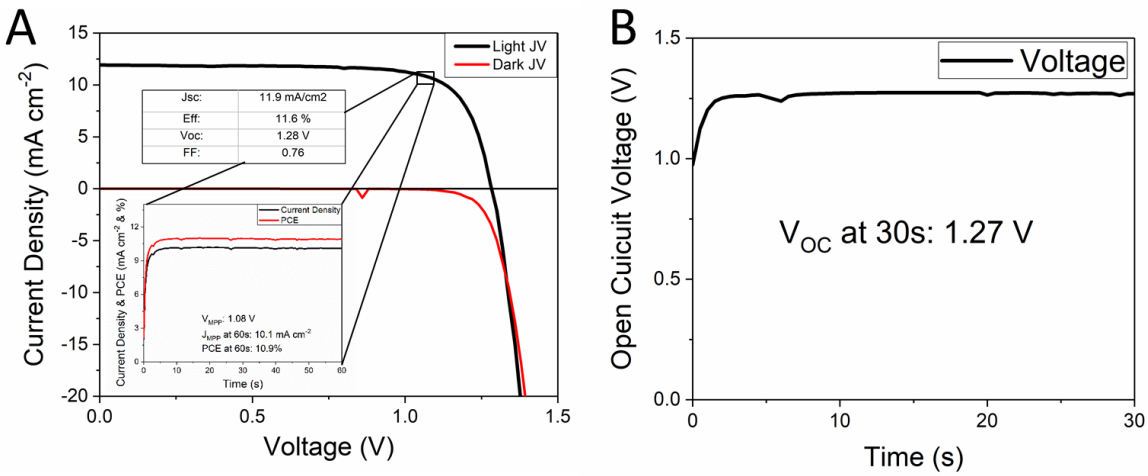

Figure S3 Current-voltage characteristic of a SnO_2/PCBM/$FA_{0.83}Cs_{0.17}Pb(Br_{0.7}I_{0.3})_3$/Spiro-OMeTAD perovskite solar cell with 2% mol. potassium (K^+) additive. A) Forward bias to short-circuit current-voltage curve measured under simulated air-mass (AM) 1.5, using a 0.25V/s scan rate. The inset figure shows the photocurrent density and power conversion efficiency measured at the maximum power point for a 60s time span. **B)** Stabilized open circuit voltage (V_{oc}) of $FA_{0.83}Cs_{0.17}Pb(Br_{0.7}I_{0.3})_3$ heterojunction perovskite solar cell.

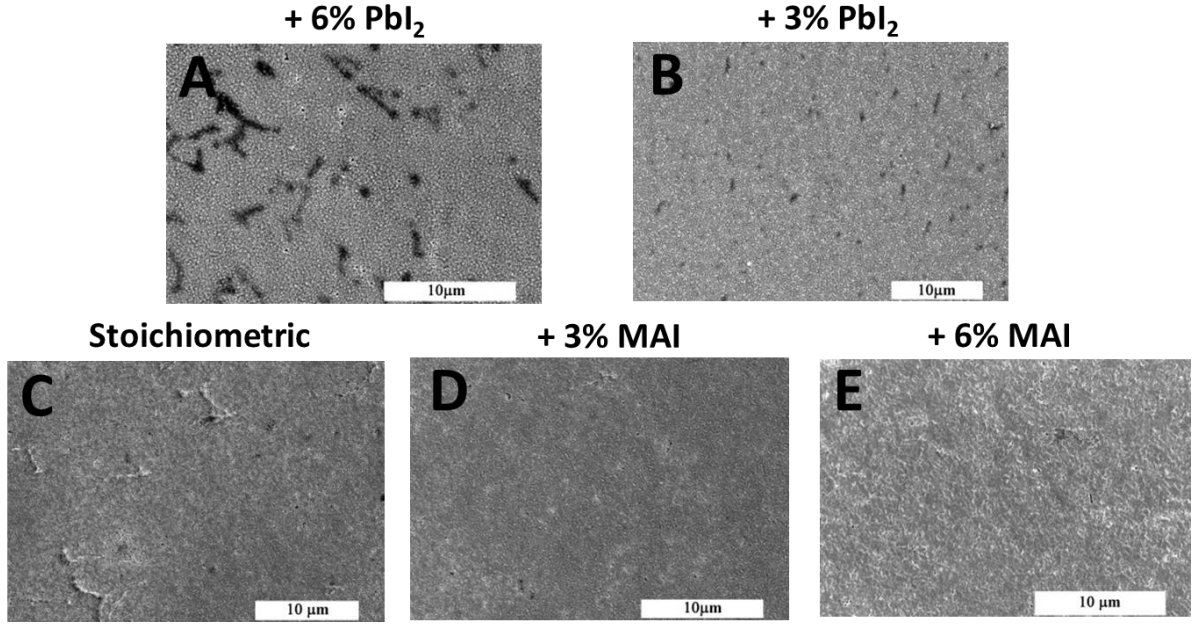

Figure S4 Scanning electron microscopy (SEM) image of the top view of $MAPbI_3$ thin film deposited on top of the front-cell and interlayer, prepared using an acetonitrile(CH_3CN)/methylamine(CH_3NH_2) (ACN/MA) solvent system, ranging from excess 6% PbI_2 to excess 6% MAI.

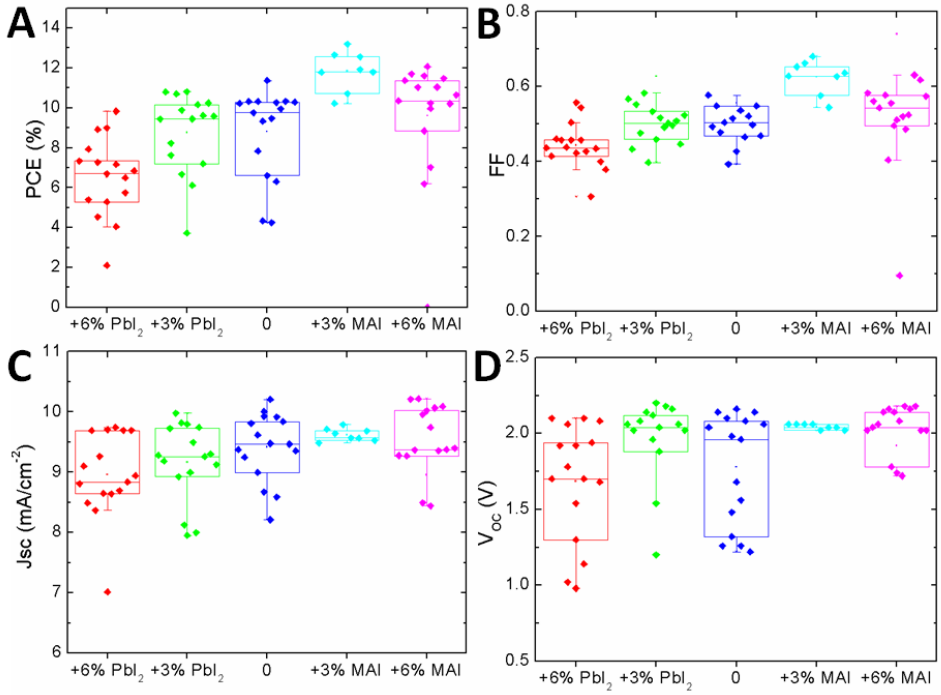

Figure S5 Impact of varying the composition of A to B-site cations of the ACN/MA $MAPbI_3$ perovskite system in the SnO_2/PCBM/$FA_{0.83}Cs_{0.17}Pb(Br_{0.7}I_{0.3})_3$/Spiro-OMeTAD/PEDOT:PSS/ITO NPs/PCBM/$MAPbI_3$/Spiro-OMeTAD tandem architecture structure. A) Power conversion efficiency B) Fill-factor C) Short-circuit current density D) Open-circuit voltage.

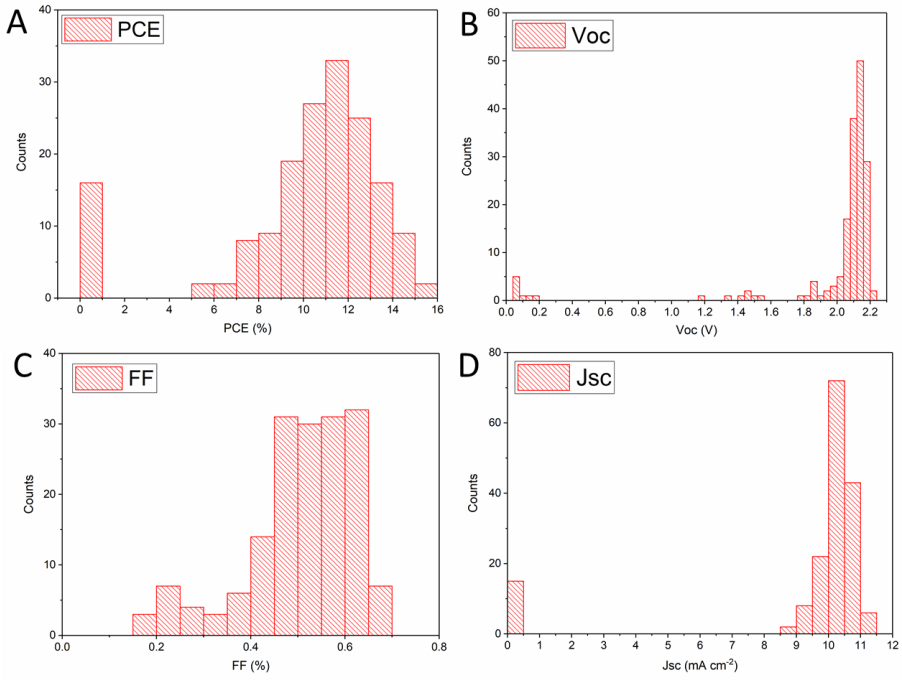

Figure S6 Histogram of the performance of the $FA_{0.83}Cs_{0.17}Pb(Br_{0.7}I_{0.3})_3$/$MAPbI_3$ tandem solar cell perovskite. A) JV Power conversion efficiency (PCE). B) Open-circuit voltage (V_{oc}). D) Fill-factor (FF). C) Short-circuit current-density (J_{sc}).

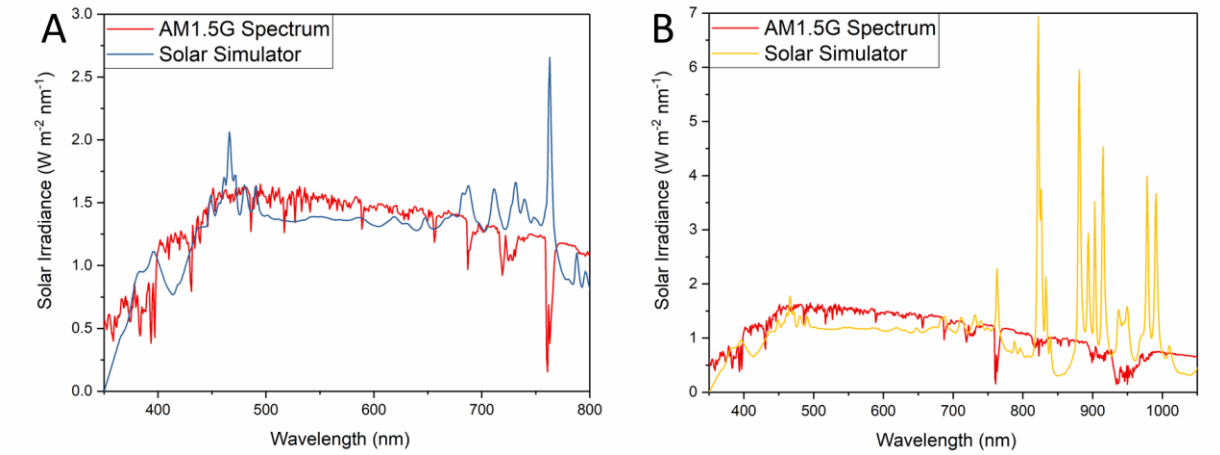

Figure S7 Measured solar simulator spectrum compared to the AM1.5G spectrum. A) Xenon lamp spectrum used for the measurement of the $FA_{0.83}Cs_{0.17}Pb(Br_{0.7}I_{0.3})_3$/$MAPbI_3$ tandem solar cell B) Xenon lamp spectrum used for the measurement of the $FA_{0.83}Cs_{0.17}Pb(Br_{0.7}I_{0.3})_3$/$MAPbI_3$/$MAPb_{0.75}Sn_{0.25}I_3$ triple-junction solar cell.

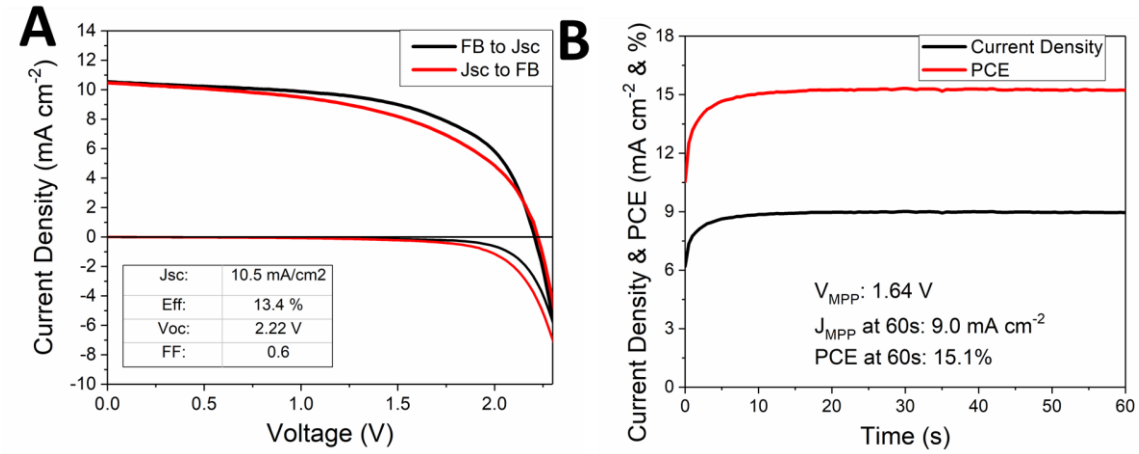

Figure S8 Device performance of a $FA_{0.83}Cs_{0.17}Pb(Br_{0.7}I_{0.3})_3$/$MAPbI_3$ tandem solar cell with the highest open circuit voltage A) Current-voltage characteristics, measured under simulated air-mass (AM) 1.5 sunlight, using a 0.25V/s scan rate. B) Photocurrent density and power conversion efficiency measured at the maximum power point for a 60 s time span. A mismatch factor of 1.004 has been applied to the PCE.

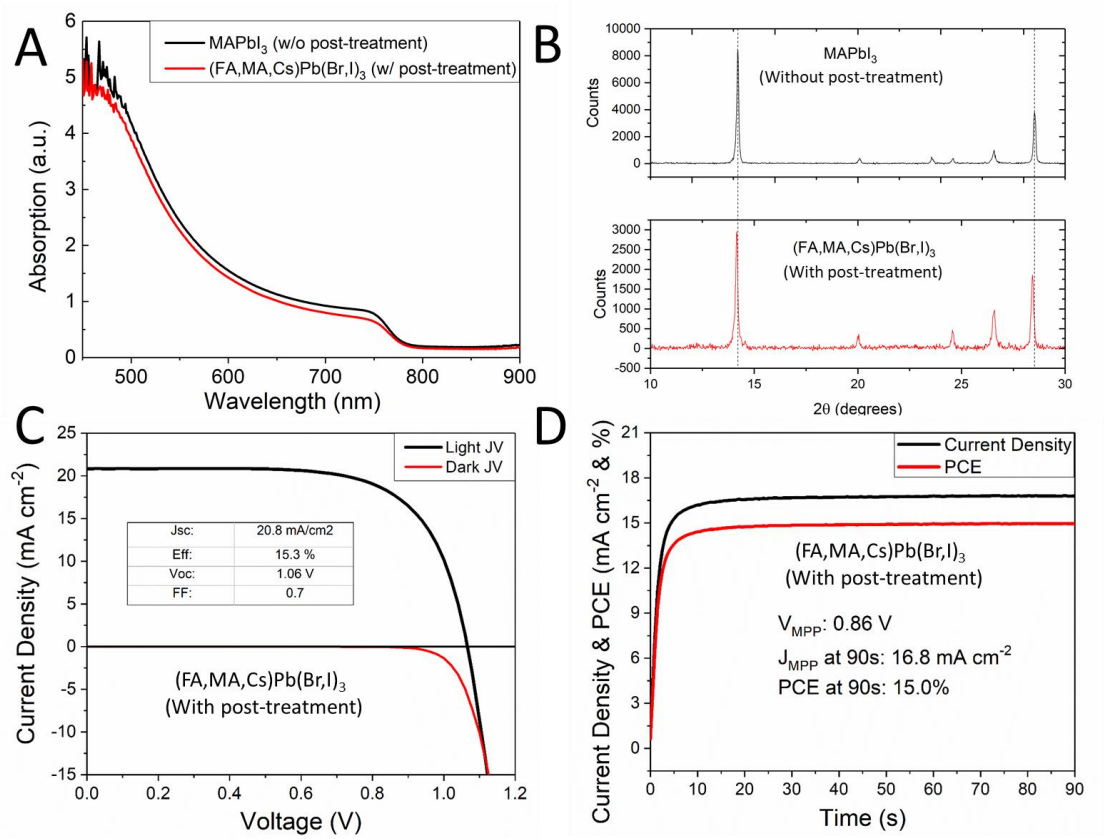

Figure S9 Impact of the FAI/CsBr in MeOH post-treatment on the absorption onset, crystal structure and device performance of the $MAPbI_3$ processed via the ACN/MA solvent system. A) Absorption spectrum and B) XRD-diffraction pattern shown before and after deposition of the FAI/CsBr in MeOH post-treatment. C) Current-voltage characteristics, measured under simulated air-mass (AM) 1.5 sunlight using a 0.25V/s scan rate. D) Photocurrent density and power conversion efficiency measured at the maximum power point for a 90 s time span. A mismatch factor of 1.004 has been applied to the PCE.

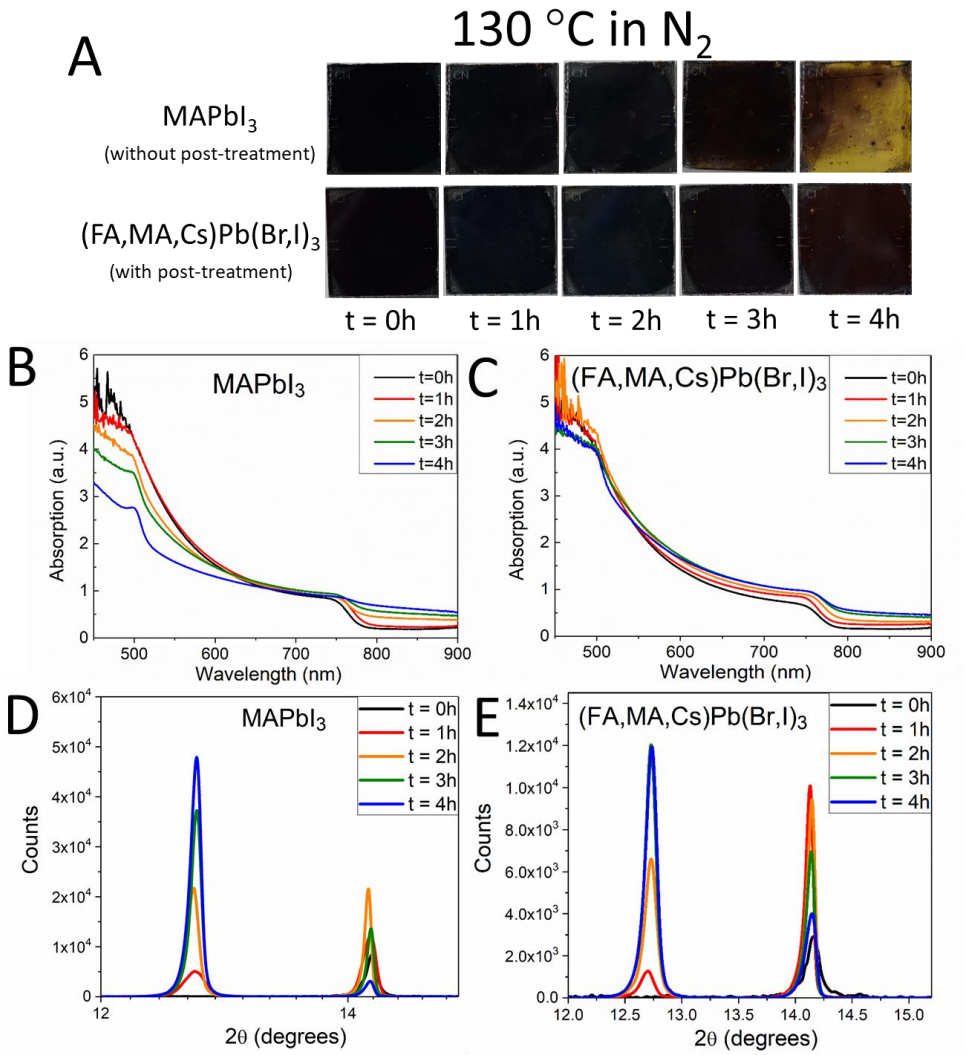

Figure S10 Impact of the FAI/CsBr in MeOH post-treatment on the thermal stability of the $MAPbI_3$ processed via the ACN/MA solvent system. A) Photographs of a $MAPbI_3$ fabricated via the ACN/MA solvent system thin film with and without the post-treatment. The perovskite films were stressed at 130° C in a nitrogen atmosphere. B,C) Ultraviolet-visible absorbance spectra of corresponding films. D,E) XRD-diffraction pattern of corresponding films.

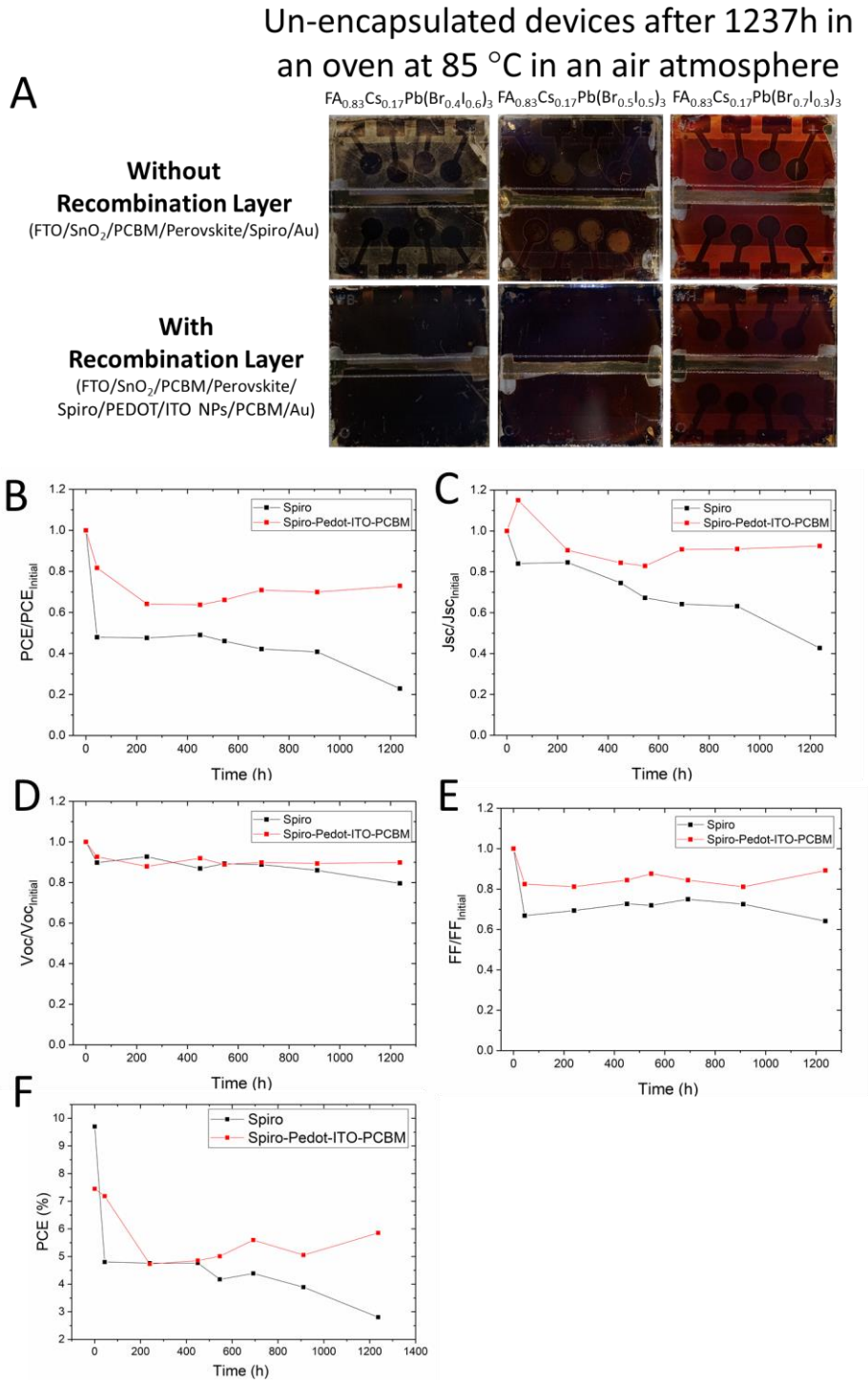

Figure S11 Impact of the added recombination layer along with the PCBM electron accepting layer on the thermal stability of the perovskite device. **The 40 devices were stressed at 85° C in an oven in an air atmosphere.** A) Photographs of $FA_{0.83}Cs_{0.17}Pb(I_{(1-y)}Br_y)_3$ devices with and without the added Pedot/ITO NPs recombination layer and the PCBM electron accepting layer. Impact of temperature on the average B) PCE/PCE$_{Initial}$, C) Jsc/Jsc$_{Initial}$, D) Voc/Voc$_{Initial}$, E) FF/FF$_{Initial}$ F) PCE.

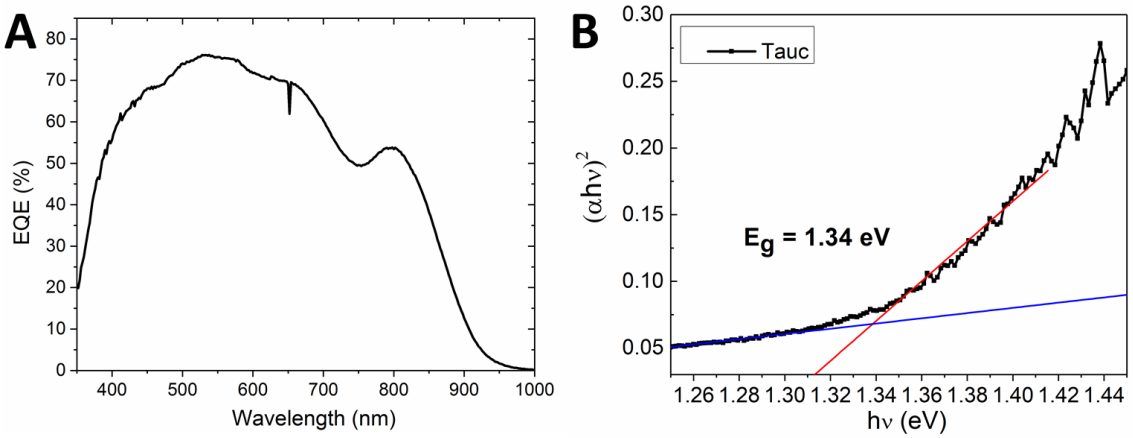

Figure S12 Characterization of $MAPb_{0.75}Sn_{0.25}I_3$ perovskite material A) External quantum efficiency (EQE) spectrum for a FTO/SnO_2/$PC_{61}BM$/$MAPb_{0.75}Sn_{0.75}I_3$/Spiro(TFSI)$_2$ solar cells architecture, measured using a 50 Ω resistive load. B) Tauc plot of $MAPb_{0.75}Sn_{0.25}I_3$ perovskite material assuming direct band gap material.

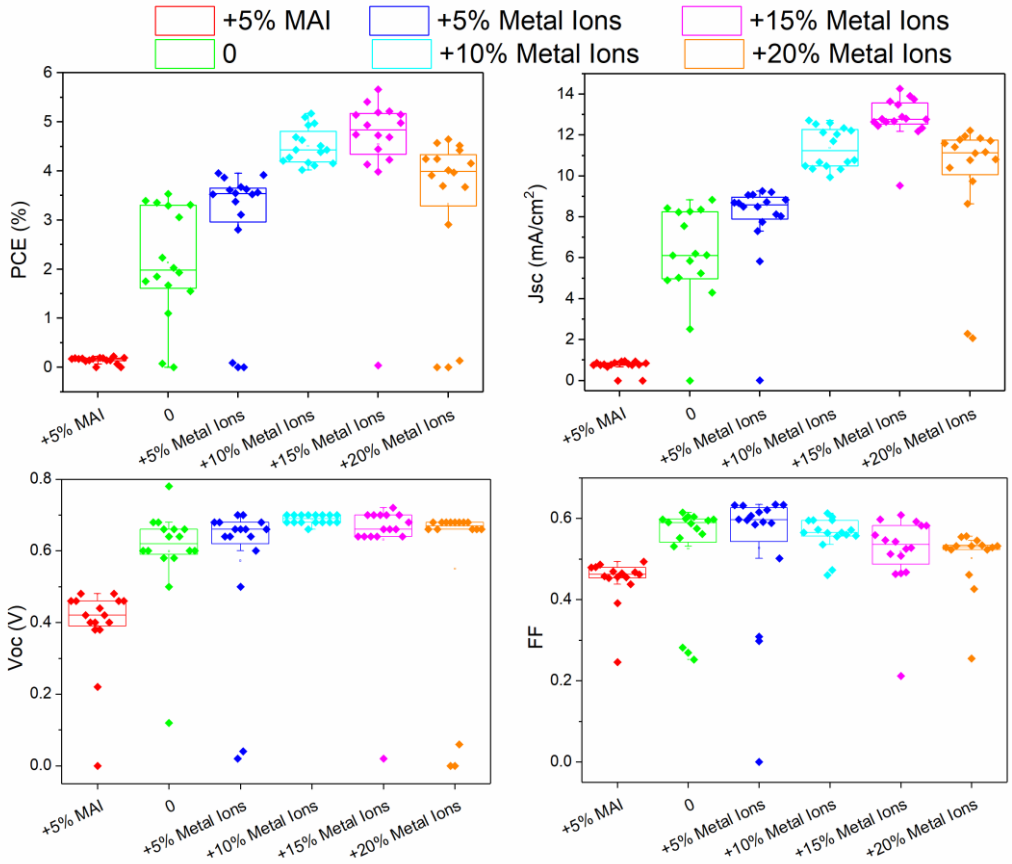

Figure S13 Impact of varying the composition of A to B-site cations of the ACN/MA $MAPb_{0.75}Sn_{0.25}I_3$ single junction perovskite system on A) power conversion efficiency B) fill-factor C) short-circuit current density D) open-circuit voltage.

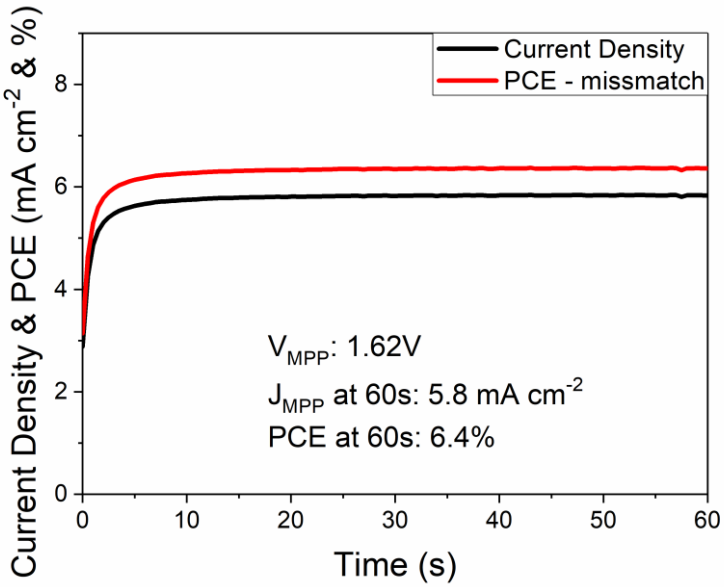

Figure S14 Device performance of a $FA_{0.83}Cs_{0.17}Pb(Br_{0.7}I_{0.3})_3/MAPbI_3/MAPb_{0.75}Sn_{0.25}I_3$ triple-junction solar cells with the highest open circuit voltage A) Current-voltage characteristic measured under simulated sunlight, , with an equivalent irradiance of 98.8 mW cm^{-2} and a spectral mismatch factor of 1.486, measured at a 0.25 V/s scan rate. B) Photocurrent density and power conversion efficiency measured at the maximum power point for a 60s time span.

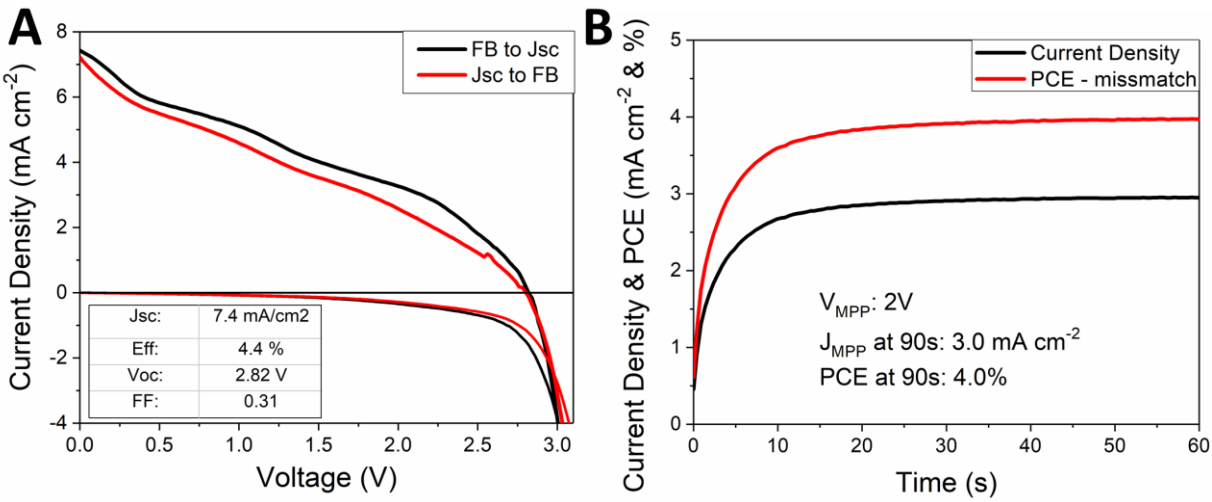

Figure S15 Device performance of a $FA_{0.83}Cs_{0.17}Pb(Br_{0.7}I_{0.3})_3/MAPbI_3/MAPb_{0.75}Sn_{0.25}I_3$ triple-junction solar cells with the highest open circuit voltage A) Current-voltage characteristic measured under simulated sunlight, with an equivalent irradiance of 98.8 mW cm^{-2} and a spectral mismatch factor of 1.486, measured at a 0.25 V/s scan rate. B) Photocurrent density and power conversion efficiency measured at the maximum power point for a 60s time span.

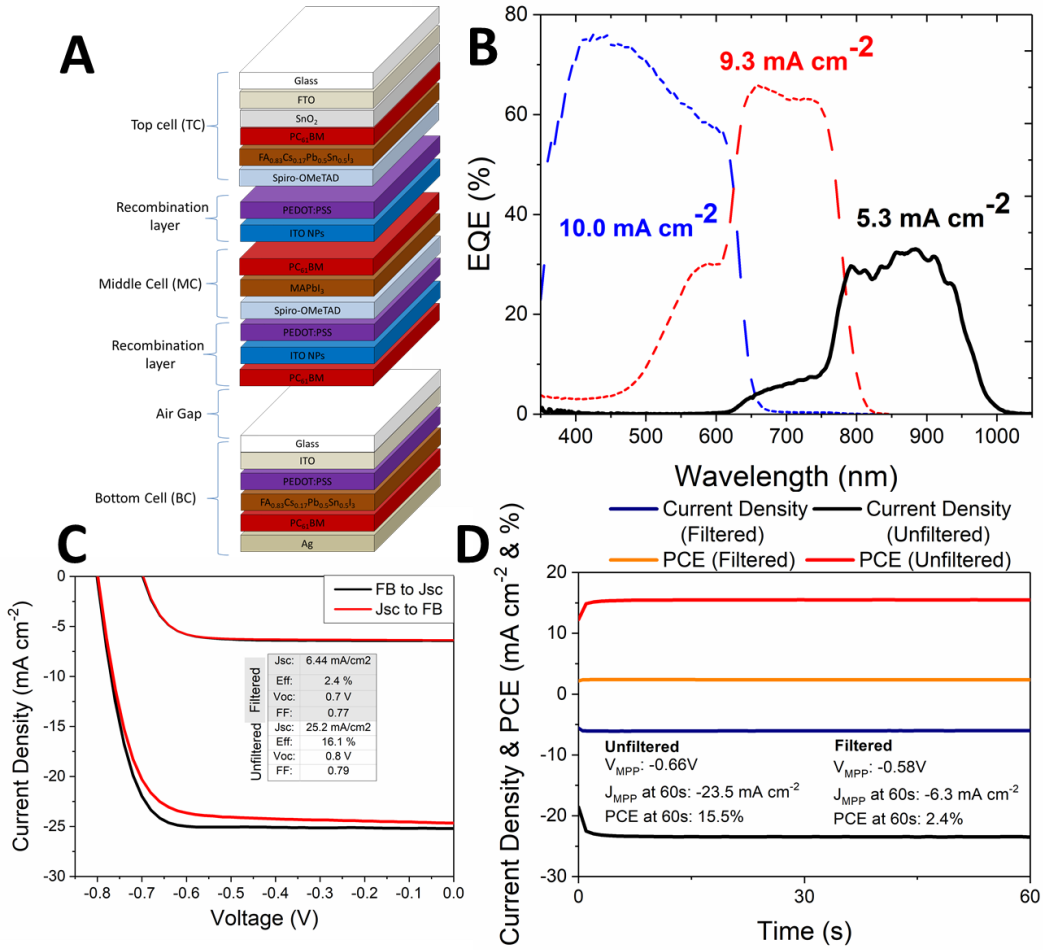

Figure S16 Architecture and device characterization of a $FA_{0.83}Cs_{0.17}Pb_{0.5}Sn_{0.5}I_3$ filtered with a $FA_{0.83}Cs_{0.17}Pb(Br_{0.7}I_{0.3})_3/MAPbI_3$ dual-junction solar cells. A) Schematics showing the filtering of the $FA_{0.83}Cs_{0.17}Pb_{0.5}Sn_{0.5}I_3$ perovskite with an all-solution processed perovskite/perovskite two-terminal (2T) $FA_{0.83}Cs_{0.17}Pb(Br_{0.7}I_{0.3})_3/MAPbI_3$ tandem perovskite solar cell. B) EQE spectrum for a $FA_{0.83}Cs_{0.17}Pb_{0.5}Sn_{0.5}I_3$ (solid line) filtered with a $FA_{0.83}Cs_{0.17}Pb(Br_{0.7}I_{0.3})_3/MAPbI_3$ dual-junction solar cells, and the integrated current density for the tandem perovskite solar cell. We also show alongside, the EQE spectrum for each sub-cell of the $FA_{0.83}Cs_{0.17}Pb(Br_{0.7}I_{0.3})_3/MAPbI_3$ tandem perovskite solar cell with an opaque electrode, and the integrated current density for the tandem perovskite solar cell. C) J-V characteristics for the champion a $FA_{0.83}Cs_{0.17}Pb_{0.5}Sn_{0.5}I_3$ unfiltered and filtered with a $FA_{0.83}Cs_{0.17}Pb(Br_{0.7}I_{0.3})_3/MAPbI_3$ dual-junction solar cell fabricated, measured at a 0.25 V/s scan rate. C) Photocurrent density and power conversion efficiency measured at the maximum power point for a 60s time span of the $FA_{0.83}Cs_{0.17}Pb_{0.5}Sn_{0.5}I_3$ unfiltered and filtered solar cell. A mismatch factor of 1.486 has been applied to the PCE.

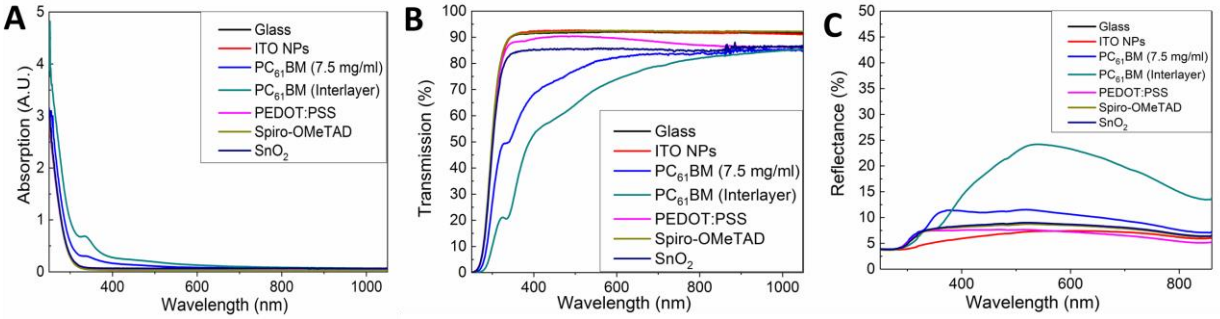

Figure S17 Optical properties of the recombination interlayer and hole and electron accepting layers. A) Absorption measured from 250nm to 1050nm of glass, indium-tin oxide nanoparticles (ITO NPs), phenyl-C61-butyric acid methyl ester ($PC_{61}BM$), phenyl-C61-butyric acid methyl ester ($PC_{61}BM$), poly(3,4-ethylenedioxythiophene) polystyrene sulfonate (PEDOT:PSS), (2,2′,7,7′-tetrakis(N,N′-di-p-methoxyphenylamine)-9,9′-spirobifluorene) (Spiro-OMeTAD). B) Transmission measurement C) Reflectance measurement.

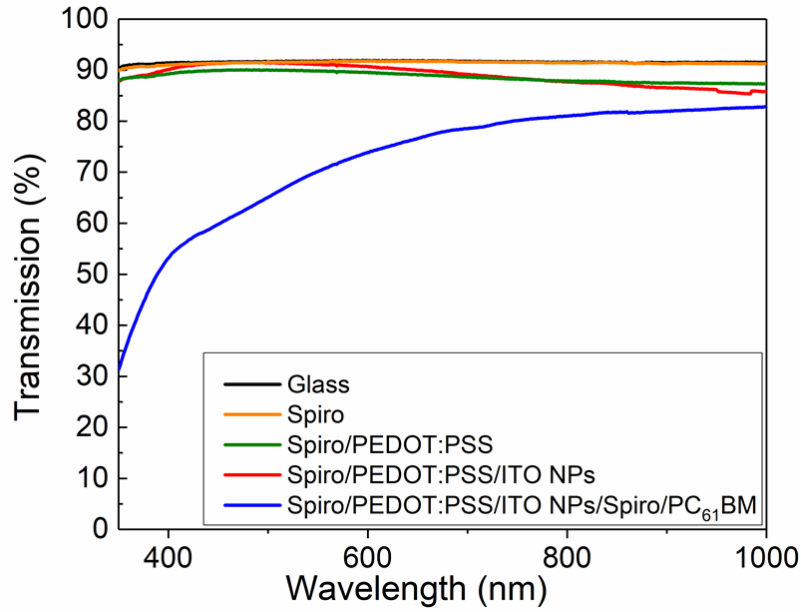

Figure S18 Transmission measurement of sequentially deposition of the hole accepting layer, the recombination interlayer and electron accepting layers.

To calculate the mismatch factor (M) of the tandem solar cell, we employed the give formula[1]:

$$M = \frac{\int E_R(\lambda)\, S_R(\lambda) d\lambda}{\int E_S(\lambda) S_R(\lambda) d\lambda} \; \frac{\min(\int E_S(\lambda)\, S_{top}(\lambda) d\lambda\,, \int E_S(\lambda)\, S_{bot}(\lambda) d\lambda)}{\min(\int E_R(\lambda)\, S_{top}(\lambda) d\lambda\,, \int E_R(\lambda)\, S_{bot}(\lambda) d\lambda)}$$

Where, E_R is the spectral irradiance of the AM1.5G spectrum, S_R is the spectral response of the silicon reference cell, E_S is the relative spectral irradiance of the Abet Class AAB sun 2000 solar simulator, S_{top} is the spectral response of the front cell, S_{bot} is the spectral response of the bot cell.

Architecture	Uncorrected mismatch factor	Mismatch factor after lamp adjusted	Filter for Reference cell
Tandem solar cell	1.050	1.004	KG5
Triple-junction solar cell	1.507	1.486	KG2

Table S1 Table of the calculated mismatch factors for the tandem perovskite solar cell and the triple-junction perovskite solar cell.

Architecture	Spectral Mismatch Factor	Raw efficiency – Uncorrected for Spectral Mismatch	Reported efficiency – Corrected for Spectral Mismatch
Tandem	1.004	15.3%	15.2%
Triple-junction	1.486	9.9%	6.7%

Table S2 Table showing the raw uncorrected efficiency, along with the reported corrected for spectral mismatch for both the tandem and the triple-junction perovskite solar cell.

EXPERIMENTAL SECTION

Front Cell (TC) Fabrication: Glass/FTO/SnO_2/$PC_{61}BM$/$FA_{0.83}Cs_{0.17}Pb(Br_{0.7}I_{0.3})_3$/Spiro-OMeTAD
Substrate Preparation: Devices were fabricated on fluorine-doped tin oxide (FTO) coated glass (Pilkington, 15Ω □$^{-1}$). Initially, FTO was removed at specific regions where the anode contact will be deposited. This FTO etching was done using a 2M HCl and zinc powder. Substrates were then cleaned with Hellmanex detergent and rinsed with water. Finally, the substrates were then cleaned sequentially in acetone, isopropyl alcohol (IPA), and dried with a compressed air gun.

Tin Oxide (SnO_2) layer fabrication: Immediately prior to spin coating, we prepared a SnO_2 precursor solution comprised of 17.5mg ml^{-1} tin(IV) chloride pentahydrate ($SnCl_4 \cdot 5H_2O$) (Sigma-Aldrich) dissolved in anhydrous 2-propanol (IPA). The solution was spin-coated in nitrogen at 3000 rpm for 30 s, with a ramp of 200 rpm/s. The substrates were then dried in nitrogen at 100 °C for 10 min. A subsequent annealing step was done in air at 180 °C for 90 min.

$PC_{61}BM$ layer fabrication: A Phenyl-C61-butyric acid methyl ester ($PC_{61}BM$) precursor solution was prepared by dissolving a 7.5 mg ml^{-1} $PC_{61}BM$ (99%, solenne) in anhydrous chlorobenzene (CB) (Sigma). We doped the $PC_{61}BM$ using dihydro-1H-benzoimidazol-2-yl (N-DBI) derivatives, specifically 3-dimethyl-2-phenyl-2,3-dihydro-1H-benzoimidazole (N-DMBI).[2–7] We doped the $PC_{61}BM$ precursor solution with N-DMBI at a 0.25% wt%. This solution was then filtered using a 0.45 □m PTFE filter. We spin coated this solution in a nitrogen-filled glovebox at 2000 rpm for 20s with a ramp rate of 1000 rpm/s, and annealed the substrate at 80 °C for 10 min.

FAI synthesis: Formamidinium iodide (FAI) was synthesized by dissolving formamidine acetate salt (99%, Sigma-Aldrich) in a 1.5x molar excess of hydriodic acid (HI), 57 wt. % in H_2O, distilled, stabilized, 99.95% (Sigma-Aldrich). After addition of acid the solution was left stirring for 10 minutes at 50 °C. Upon drying in a large glass dish at 100°C for 2h, a yellow-white powder was formed. This was then washed three times with diethyl ether. The power was later dissolved in anhydrous ethanol (99.5%, Sigma-Aldrich) and heated at 120 °C in a N_2-rich atmosphere to obtain a supersaturated solution. Once fully dissolved, the solution was then slowly cooled to room temperature in a N_2-rich atmosphere, until recrystallization occured. The recrystallization process formed white flake-like crystals. The solution was then placed and in a refrigerator at 4 °C, after which it was transferred to a freezer for further crystallization. The powder was later washed with diethyl ether three times. Finally, the powder was dried overnight in a vacuum oven at 50 °C.

$FA_{0.83}Cs_{0.17}Pb(Br_{0.7}I_{0.3})_3$ with 2% K additive perovskite precursor solution preparation: FA/Cs (formamidinium/Cs) with 2% K additive perovskite solutions were prepared by dissolving the precursor salts in anhydrous N,N-dimethylformamide (DMF) to obtain a stoichiometric solution with the desired $FA_{0.83}Cs_{0.17}Pb(Br_{0.7}I_{0.3})_3$ composition and 2% K additive using a molar ratio of 30% to 70% KI to KBr. The precursor solution was prepared using the following precursor salts: formamidinium iodide (FAI), cesium iodide (CsI) (99.9%, Alfa Aesar), lead iodide (PbI_2) (99%, Sigma-Aldrich), lead bromide ($PbBr_2$) (98%, Alfa Aesar), potassium iodide (KI) (99%, Sigma-Aldrich), potassium bromide (99%, KBr) (Sigma-Aldrich). 27.2 µl/ml of hydroiodic acid (HI) (57 wt. % in H_2O, distilled, stabilized, 99.95%, Sigma-Aldrich) and 54.8 µl/ml of hydrobromic (HBr) (48 wt. % in H_2O) was added to 1ml of 0.75 M precursor solutions. After the addition of the acids, the perovskite precursor solution was aged for 2 days under a nitrogen atmosphere.

$FA_{0.83}Cs_{0.17}Pb(Br_{0.7}I_{0.3})_3$ perovskite layer preparation: This aged precursor perovskite solution was spin-coated in a nitrogen-filled glovebox at 1200 rpm for 45s with a 600 rpm/s ramp rate. The films were dried inside a N_2 glovebox on a hot plate at a temperature of 70 °C for 1 minute. The films were then annealed in an oven in an air atmosphere at 185°C for 90 minutes. During this annealing process, the samples were covered with a large glass container to prevent dust contamination.

Spiro-OMeTAD hole-transporting layer fabrication: The electron-blocking layer was deposited with a 72.5mg/ml of 2,2',7,7'-tetrakis-(N,N-di-p-methoxyphenylamine)9,9'-spirobifluorene (spiro-OMeTAD) (Lumtec) solution in chlorobenzene. Additives of 38µl of lithium bis(trifluoromethanesulfonyl)imide (170mg/mL in 1-butanol solution) per 1ml of spiro-OMeTAD solution and 21µl of 4-tert-butylpyridine (TBP) per 1mL of spiro-OMeTAD solution. The samples were left to oxidize in a desiccator for 24h. Spin-coating was carried out in a nitrogen-filled glovebox at 2000rpm for 20s with a ramp rate of 1000 rpm/s.

Recombination Interlayer layer fabrication (for both TC/MC and MC/BC): PEDOT:PSS/ITO NPs
The interlayer is fabricated using both PEDOT:PSS (PH 1000) in water (Heraeus Clevios) and indium-tin oxide, 30 wt. % in isopropanol (IPA), (ITO) <100nm nanoparticles (NPs) dispersion (Sigma), as precursor solutions.
We first deposit a thin layer of PEDOT:PSS directly on top of the existing spiro-OMeTAD layer. The PEDOT:PSS precursor solution was prepared immediately prior to spin coating, by diluting PEDOT:PSS (PH 1000) in anhydrous 2-propanol (IPA) at a volume ratio of 1 to 1.5 (PEDOT:PSS to IPA) and then filtered with a 2.7 □m GF/D membrane filter (Whatman). The substrates were preheated at 80 °C, and we then dynamically spin coated the diluted PEDOT:PSS solution, in a dry air atmosphere <10% relative humidity (RHM), at a speed of 6000 rpm for 20 s, and then annealed for at 80 °C for 10 min.
We then deposited the ITO NPs layer. We prepared the ITO NPs precursor solution by diluting the 30 wt. % in IPA down to 1 wt. % in IPA. The diluted solution was sonicated, in a sonication bath, for 15 m prior to deposition. We dynamically spin coated the diluted ITO NPs solution, in a dry air atmosphere <10% relative humidity (RHM), at a speed of 6000 rpm for 20 s, and then annealed for at 80 °C for 10 m.

Middle Cell (MC) Fabrication: $PC_{61}BM/MAPbI_3$/Spiro-OMeTAD
$PC_{61}BM$ layer fabrication: A Phenyl-C61-butyric acid methyl ester ($PC_{61}BM$) precursor solution was prepared by dissolving a 30 mg ml^{-1} $PC_{61}BM$ (99%, solenne) in a mixture of anhydrous chlorobenzene (CB) (sigma) and anhydrous chloroform (CF) solvents. The solvents were mixed at a volume ratio of 2 to 1, CB to CF. We doped the $PC_{61}BM$ using dihydro-1H-benzoimidazol-2-yl (N-DBI) derivatives, specifically 3-dimethyl-2-phenyl-2,3-dihydro-1H-benzoimidazole (N-DMBI).[2–7] We doped the $PC_{61}BM$ precursor solution with N-DMBI at a 0.25 wt%. This solution was then filtered using a 0.45 □m PTFE filter. The substrates were preheated at 80 °C, we then dynamically spin coated this solution in a dry air atmosphere <10% relative humidity (RHM) at 4000 rpm for 20s, and annealed the substrate at 80 °C for 10 min.

ACN/MA $MAPbI_3$ perovskite precursor solution preparation:
In this work, we found that controlling the MA content in the acetonitrile(CH_3CN)/methylamine(CH_3NH_2) (ACN/MA) $MAPbI_3$ solution resulted in better tandem performance with higher reproducibility. Excess MA in the ACN/MA $MAPbI_3$ solution can potentially percolate through pinholes of thin imperfect interlayers, thus partially or completely dissolving the underlying junction. Thus, solutions with the minimal amount of MA required to dissolve the perovskite were employed. Controlling the MA content in the solution can potentially be done by controlling the MA flow rate and stirring speed, however, precisely controlling these parameters was sometimes challenging. Instead, we prepared two ACN $MAPbI_3$ dispersions, one with excess MA content resulting in a full ACN/MA $MAPbI_3$ solution, and another ACN $MAPbI_3$ dispersion without any MA. Immediately prior to spin coating, we slowly add the ACN/MA $MAPbI_3$ with excess MA to the ACN $MAPbI_3$ dispersion until this dispersion is fully dissolved, and becomes a full solution. The resulting solution is an ACN/MA $MAPbI_3$ solution at its critical solubility point. The preparations of the ACN/MA $MAPbI_3$ solution and the ACN $MAPbI_3$ dispersion are described below.
The ACN $MAPbI_3$ perovskite precursor solution without any MA was prepared, under nitrogen, using precursor salts methylammonium iodide (MAI) (Dyesol) and lead iodide (PbI_2) (TCI) added into anhydrous acetonitrile (ACN) (Sigma Aldrich) at a concentration of 1.03 M for MAI and 1 M for PbI_2, resulting in a non-stoichiometric solution (1.03:1 MAI:PbI_2). This solution was then sonicated, in a sonication bath, for 1 h in order to fully react the MAI with the PbI_2, a black perovskite dispersion is then seen at the bottom of the ACN filled vial.

The ACN/MA $MAPbI_3$ perovskite precursor solution was prepared using an adapted method described by Noel et al.[8] We first prepare an ACN/MA $MAPbI_3$ perovskite precursor solution with the identical preparation method as described above. In order to dissolve the perovskite in ACN, a solution of methylamine (MA) in ethanol (Sigma Aldrich, 33 wt%) was placed into an aerator which was kept in an ice bath. Nitrogen was then bubbled into the solution, thus degassing the solution of MA. The MA gas which was produced was then passed through a drying tube filled with a desiccant (Drietire and CaO). The gas was bubbled into the black dispersion, while vigorously stirring the ACN/MA $MAPbI_3$ dispersion using a large magnetic stir bar at a speed of approximately 700 rpm. The dispersion was bubbled for 15 minutes, which resulted in a full dissolution of the black perovskite particles, resulting in a clear, light yellow solution. We note this solution has an "excess" amount of MA in the ACN/MA $MAPbI_3$ solution.

ACN/MA $MAPbI_3$ perovskite layer preparation: The ACN/MA $MAPbI_3$ precursor perovskite solution (at it's critical solubility point) is immediately dynamically spin coated in a dry air atmosphere <10% relative humidity (RHM) at 5000 rpm for 20s. A post treatment of methylammonium chloride (MACl) was then carried out by dynamically spincoating at 6000 rpm for 20s a 50 µl of MACl (Alfa Aesar, 2 mg/ml in isopropanol). The films were then annealed in an oven in an air atmosphere at 80 °C for 90 minutes. During this annealing process, the samples were covered with a large glass container to prevent dust contamination.

ACN/MA $MAPbI_3$ perovskite layer preparation with FAI/CsBr post-treatment: The ACN/MA $MAPbI_3$ precursor perovskite solution (at it's critical solubility point) is immediately dynamically spin coated in a dry air atmosphere <10% relative humidity (RHM) at 5000 rpm for 20s. A formamidinium iodide (FAI) and cesium bromide (CsBr) post-treatment was then carried out by dynamically spincoating a 50 µl of a 0.2M solution of FAI/CsBr (83/17, molar ratio) dissolved in methanol (MeOH), at 6000 rpm for 20s. The films are annealed for 10 minutes at 80 °C. After cooling the film to room temperature, a 200 µl isopropanol solution was dynamically spin coated at 6000 rpm for 20s, to remove excess cations. The films were then annealed in an oven in an air atmosphere at 80 °C for 90 minutes. During this annealing process, the samples were covered with a large glass container to prevent dust contamination.

Spiro-OMeTAD hole-transporting layer fabrication: The electron-blocking layer was deposited by dynamically spin coating a 85mg/ml of 2,2',7,7'-tetrakis-(N,N-di-p-methoxyphenylamine)9,9'-spirobifluorene (spiro-OMeTAD) (Lumtec) solution in chlorobenzene. Additives of 20µl of lithium bis(trifluoromethanesulfonyl)imide (520mg/mL in acetonitrile solution) per 1ml of spiro-OMeTAD solution and 33µl of 4-tert-butylpyridine (*t*BP) per 1mL of spiro-OMeTAD solution. Spin-coating was done dynamically and carried out in a dry air atmosphere <10% relative humidity (RHM) at 2000 rpm for 30s. The samples were left to oxidize in a desiccator for 24h.

Rear Cell (BC) Fabrication: $PC_{61}BM/MAPb_{0.75}Sn_{0.25}I_3/Spiro(TFSI)_2$

$PC_{61}BM$ layer fabrication: A Phenyl-C61-butyric acid methyl ester ($PC_{61}BM$) precursor solution was prepared by dissolving a 30 mg ml^{-1} $PC_{61}BM$ (99%, solenne) in a mixture of anhydrous chlorobenzene (CB) (sigma) and anhydrous chloroform (CF) solvents. The solvents were mixed at a volume ratio of 2 to 1, CB to CF. We doped the $PC_{61}BM$ using dihydro-1H-benzoimidazol-2-yl (N-DBI) derivatives, specifically 3-dimethyl-2-phenyl-2,3-dihydro-1H-benzoimidazole (N-DMBI).[2–7] We doped the $PC_{61}BM$ precursor solution with N-DMBI at a 0.25% wt%. This solution was then filtered using a 0.45 □m PTFE filter. The substrates were preheated at 80 °C, we then dynamically spin coated this solution in a dry air atmosphere <10% relative humidity (RHM) at 4000 rpm for 20s, and annealed the substrate at 80 °C for 10 min.

ACN/MA $MAPb_{0.75}Sn_{0.25}I_3$ perovskite precursor solution preparation:

To obtain a mixed-metal ACN/MA $MAPb_{0.75}Sn_{0.25}I_3$ perovskite precursor solution, we mixed an ACN/MA $MAPbI_3$ with an ACN $MAPb_{0.5}Sn_{0.5}I_3$ (without any MA) at a 1:1 volume ratio, resulting in an ACN/MA $MAPb_{0.75}Sn_{0.25}I_3$.

The ACN/MA $MAPb_{0.5}Sn_{0.5}I_3$ solution perovskite precursor solution, without any MA was prepared, under nitrogen, using precursor salts methylammonium iodide (MAI) (Dyesol), lead iodide (PbI_2) (TCI), and anhydrous tin iodide (SnI_2) beads (TCI) added into anhydrous acetonitrile (ACN) (Sigma Aldrich) at a concentration of 0.8 M for MAI, 0.46 M for PbI_2 and 0.46 M for SnI_2, resulting in a non-stoichiometric solution with 15% excess metal salts (1:1.15 MAI:PbI_2+SnI_2). This solution was then stirred under nitrogen at 70 °C for 1h, in order to fully react the MAI with the mixed metals, a black perovskite dispersion is then seen at the bottom of the ACN filled vial.

The ACN/MA $MAPbI_3$ perovskite precursor solution was prepared using an adapted method described by Noel et al.[8] We first prepare a ACN/MA $MAPbI_3$ perovskite precursor solution at a 0.8 M for MAI and 0.46 M for PbI_2, resulting in a non-stoichiometric solution with 15% excess metal salts (1:1.15 MAI:PbI_2). In order to dissolve the perovskite in ACN, a solution of methylamine (MA) in water H_2O (Sigma Aldrich, 40 wt%) was placed into an aerator which was kept in an ice bath. Nitrogen was then bubbled into the solution, thus degassing the solution of MA. The MA gas which was produced was then passed through a drying tube filled with a desiccant (Drietire and CaO). The gas was bubbled into the black dispersion, while vigorously stirring the ACN/MA $MAPbI_3$ dispersion using a large magnetic stir bar at a speed of approximately 700 rpm. The dispersion was bubbled for 15 minutes, which resulted in a full dissolution of the black perovskite particles, resulting in a clear, light yellow solution. We note this solution has an "excess" amount of MA in the ACN/MA $MAPbI_3$ solution. The solution was then stored in nitrogen for approximately 3 h with activated 3 Å molecular sieves to remove any H_2O that was introduced during the MA bubbling process.

ACN/MA $MAPb_{0.75}Sn_{0.25}I_3$ perovskite layer: This precursor perovskite solution is immediately dynamically spin coated in a nitrogen glovebox at 5000 rpm for 20s. A second subsequent spin coating step was used to deposit a methylammonium chloride (MACl) post treatment. A 2 mg ml^{-1} solution of MACl in IPA was dynamically spin coated at 6000rpm for 20s. The films were then annealed in nitrogen at 80°C for 90 minutes.

$Spiro(TFSI)_2$ synthesis: The $Spiro(TFSI)_2$ hole-transporting layer used for the $MAPb_{0.75}Sn_{0.25}I_3$ perovskite was prepared using an adapted method described by Nguyen et al.[9] We first dissolved 2,2',7,7'-tetrakis-(N,N-di-p-methoxyphenylamine)9,9'-spirobifluorene (spiro-OMeTAD) (Lumtec) solution in chlorobenzene (CB) at a 2 mg ml^{-1} concentration. Separately, we dissolved the Silver(I) bis(trifluoromethanesulfonyl)imide (Ag-TFSI) in methanol at a 100 mg ml^{-1}. We slowly mixed identical volumes of both solutions together, while stirring. The final molar ratio is 1 to 0.95 (spiro-OMeTAD to Ag-TFSI). We then left the mixed solution stirring overnight. We filtered the solution with a 0.2 □m PTFE filter to remove the Ag colloids. We used a rotary evaporation to remove CB until approximately 5% of the original volume is left. We then added toluene to the remaining flask at a volume of 50% of the initial CB volume. We placed the solution in a refrigerator for 24h, where a fine black powder precipitated. Once, the black powder fully settled, we removed excess toluene using a glass frit filter. We washed the powder with a cold 4 °C toluene. Once the powder was dry, we prepared a 20 mg ml^{-1} in methanol solution. This black powder should not have low solubility in methanol, which starts the precipitation process. We refrigerated the solution at 4 °C overnight. The black powder collected at the bottom of the vial. We removed the excess toluene using a glass frit filter, and washed with 4 °C methanol. Once dry, we collected and weighed the $Spiro(TFSI)_2$ powder.

Spiro-OMeTAD doped with 10 wt.% $Spiro(TFSI)_2$ hole-transporting layer fabrication: The electron-blocking layer was deposited by dynamically spin coating a $spiro(TFSI)_2$ doped spiro-OMeTAD at 2000 rpm for 30s in a nitrogen glovebox. This precursor solution was prepared with a 72.5 mg ml^{-1} wt.% spiro solution composed of a 7.25 mg ml^{-1} $Spiro(TFSI)_2$ and a 65.25 mg ml^{-1} 2,2',7,7'-tetrakis-(N,N-di-p-methoxyphenylamine)9,9'-spirobifluorene (spiro-OMeTAD) (Lumtec) solution in chlorobenzene. No additives were added to the spiro-OMeTAD solution.

Rear Cell (BC) Fabrication: PEDOT:PSS/$FA_{0.83}Cs_{0.17}Pb_{0.5}Sn_{0.5}I_3$/$PC_{61}BM$/BCP

$FA_{0.83}Cs_{0.17}Pb_{0.5}Sn_{0.5}I_3$ perovskite precursor preparation: A stoichiometric solution of 1.2 M $FA_{0.83}Cs_{0.17}Pb_{0.5}Sn_{0.5}I_3$ was prepared in a nitrogen atmosphere by dissolving FAI (Dyesol), CsI (99.9%, Alfa Aesar), PbI_2 (99.999%, Alfa Aesar), and SnI_2 (99.999%, Alfa Aesar) in a mixed solvent of 4:1 DMF:DMSO by volume. Also dissolved in the solution is 60 mM tin (II) fluoride (SnF_2, 99%, Sigma Aldrich) and 36 mM lead (II) thiocyanate (99.5%, Sigma Aldrich).

Device preparation: Patterned indium tin oxide (ITO) substrates were cleaned by sequentially rinsing in acetone and IPA. Once dried, the substrates were cleaned with an O_2-plasma for ten minutes. Immediately following plasma treatment, a PEDOT:PSS solution (PVP AI 4083, Heraeus, in a 1:2 volume ratio with methanol) was spincoated in ambient conditions at 4 krpm for 30 s, followed by annealing at 150 °C in ambient for 10 minutes. The devices were immediately transferred to a N_2 glovebox. Just prior to fabricating the perovskite film the PEDOT:PSS coated ITO substrates were annealed again at 120 °C for 10 minutes. The perovskite film was fabricated by spincoating the solution at 3.6 krpm for 14 s with a 6 s ramp. At 13 s after the start of the spincoating program, 200 µL of anisole was dispensed onto the spinning substrate. Once spincoating is finished, a stream of N_2 was applied to the film for 15 s and then immediately annealed at 120 °C for 10 minutes. The $PC_{61}BM$ layer was produced by dynamically spincoating 50 uL of a hot solution (90°C) of $PC_{61}BM$ (20 mg/mL dissolved in a mixed solvent of 3:1 chlorobenzene:1,2-dichlorobenzene by volume) at 2 krpm for 30 s and subsequently annealed at 90°C for 2 minutes. Once cooled to room temperature, 70 µL of a 0.5 mg/mL solution of bathocuproin (BCP, 98%, Alfa Aesar) was dynamically spincoated at 4 krpm for 20 s.

Electrode: A 100 nm silver or gold electrode was thermally evaporated under vacuum of $\approx 10^{-6}$ Torr, at a rate of ≈ 0.2 nm·s^{-1}.

Solar cell characterization: The current density–voltage (J-V) curves were measured (2400 Series SourceMeter, Keithley Instruments) under simulated AM 1.5 sunlight at approximately 100 mWcm^{-2} irradiance generated by an Abet Class AAB sun 2000 simulator, with the intensity calibrated with an NREL calibrated KG5 filtered Si reference cell. For single junctions, the mismatch factor was calculated to be less than 1%. For multi-junctions, the mismatch factor was calculated for each junction and PCE were adjusted accordingly. The active area of the solar cell is 0.0919 cm^{-2}. The forward J–V scans were measured from forward bias (FB) to short circuit (SC) and the backward scans were from short circuit to forward bias, both at a scan rate of 0.25V s^{-1}. A stabilization time of 5 seconds under 1 sun illumination and forward bias of 0.3V above the expected V_{OC} was done prior to scanning.

External quantum efficiency (EQE) characterization: The multi-junction EQEs were measured by optically biasing the sub-cells that are not being measured with a 3W 470-475 nm LED and a 3W 730-740 nm LED, for the TC and for the BC, respectively. A negative bias equal to V_{oc} of the sub-junction that is being optically biased was applied to the tandem during the measurement. This allows us to measure the response of the tandem in short-circuit condition.

Transient photoconductivity: The Nd:YAG laser excitation source tuned to 470 nm and pumped at 10 Hz with 3.7 ns pulses is used at the range of fluences to have various charge carrier density as described in the main text. This pulse light is illuminated across the entire sample area to evenly excite the film. A bias of 24 V is applied across the in-plane (lateral) electrodes. Here, since the contact resistance between perovskite film and Au electrode is fairly small compared to sample resistance, we employ a two-point probe conductivity measurement. A variable resistor is in series with sample in the circuit to always be <1% of the sample resistance. We monitored the voltage drop across a variable resistance, placed in series with the sample, using a 1MΩ input resistance oscilloscope to determine the potential drop across the two in-plane Au electrodes (4 mm channel to channel distance) in the sample. Perovskite film is scribed to have 5mm channel width, and coated with inert 200nm PMMA. Transient photoconductivity ($\sigma_{Transient-Photo}$) was calculated by the equation, $\sigma_{Transient-Photo} = \frac{V_r}{R_r \times (V_{bias} - V_r)} \times \frac{l}{w \times t}$ where, V_r is voltage drop across the resistor, R_r is variable resistor, V_{bias} is bias voltage, l is channel-channel length, w is channel width, and t is film thickness.

Modeling:

Overview

We modelled the optical properties of the stack using a generalized transfer matrix method (TMM).[10] All the calculations were done in Python with heavy use of the NumPy and SciPy libraries. The wavelength dependent complex refractive index, the layer thicknesses and the incidence angle were fed as input.

The TMM model outputs the electric field distribution in the stack. This was used to calculate Transmittance $T(E)$, Reflectance $R(E)$ and the absorption $A(E)$ in each layer. The short circuit current of each sub-cell was then determined by assuming the internal quantum efficiency to be unity:

$$J_{SC} = q \int_0^{\infty} A(E) \cdot \phi_{AM1.5}(E) \cdot dE$$

Here, $\phi_{AM1.5}(E)$ is the photon flux from the AM1.5 spectrum.

The JV curve from each sub-cell was obtained by combining this modelled J_{SC} with the electrical characteristics of state-of-art single junction cells. To do this, we parametrized the JV curves of state-of-the-art single junctions as per the single diode equivalent model:

$$J(V) = J_{sun} - J_0\left(e^{\frac{V+J(V)R_S}{nV_T}} - 1\right) - \frac{V + J(V)R_S}{R_{SH}}$$

Where n, V_T, R_S, J_0 *and* R_{SH} are respectively the electron charge, thermal voltage at 300K, series resistance, dark current, and shunt resistance. The JV curve of each multi-junction sub-cell is modelled by replacing J_{sun} in the fitted equation with the J_{SC} calculated from the multijunction stack. As the correlation between J_{sun} and other fitting parameters is negligible, we can be sure that J_{sun} can be changed without changing other parameters. The approach of Jain et al.[11] was used to solve the single diode model using the Lambert W function. After calculating the JV curves of all sub-cells, we combined them to obtain the multi-junction JV curve.[12] The maximum point is calculated from this combined JV curve.

Inputs for the Optical and Electrical Models

The refractive indices for ITO[13], FTO[14], PEDOT:PSS[15], PCBM[16], Spiro-OMeTAD[17], Ag[18], $MA_{0.4}FA_{0.6}Sn_{0.6}Pb_{0.4}I_3$[19] and $MAPbI_3$ [20] were taken from the literature. The extinction co-efficient k of $FA_{0.83}Cs_{0.17}Pb(Br_{0.7}I_{0.3})_3$ was obtained by measuring the transmittance T and the reflectance R of a thin film of thickness t on glass and using the relations:

$$\alpha = \frac{4\pi k}{\lambda}$$

$$\frac{T}{1-R} = e^{\alpha t}$$

Once $k(\lambda)$ was obtained, we parametrized it in terms of Lorentz oscillators to get an analytical representation, which was transformed into the refractive index $n(\lambda)$ via the Kramers-Kronig transform:

$$n(\lambda) = 1 + \frac{2}{\pi}\int_0^\infty \frac{E'k(E)}{E'^2 - E^2}dE'$$

The electrical characteristics for the $MAPbI_3$ [21]and the $MAPb_{0.75}Sn_{0.25}I_3$[22] are taken from best reported cells of same or similar class in the literature. For the $FA_{0.83}Cs_{0.17}Pb(Br_{0.7}I_{0.3})_3$ sub-cell, we use the JV curve of our best $FA_{0.83}Cs_{0.17}Pb(Br_{0.7}I_{0.3})_3$ single junction cell (Figure S3).

To account for the ITO nanoparticles being embedded in PCBM, we model its refractive index as a Bruggeman Effective Medium with 75% ITO and 25% PCBM. The refractive index of this effective medium is calculated by solving:

$$\frac{f_{ITO}(n_{ITO}^2 - n^2)}{(n_{ITO}^2 + 2n^2)} = \frac{(1 - f_{FTO})(n_{PCBM}^2 - n^2)}{(n_{PCBM}^2 + 2n^2)}$$

Where n_{ITO}, n_{PCBM} and f_{ITO} are respectively the complex refractive index of ITO, complex refractive index of PCBM and the fraction of ITO in the effective medium.

Tandem Simulation

$FA_{0.83}Cs_{0.17}Pb(Br_{0.7}I_{0.3})_3/MAPbI_3$ simulation - Figure A,B

The thicknesses used in the optical model are obtained from an SEM cross section of the tandem. The electrical characteristics of $FA_{0.83}Cs_{0.17}Pb(Br_{0.7}I_{0.3})_3$ and $MAPbI_3$ presented are extracted from our own single junction devices (FigureS3). The dotted JV models the performance assuming the $MAPbI_3$ performs as well as the best ACN processed $MAPbI_3$ cell in literature.

Layer	**Thickness**
Glass	2.2mm
ITO	350nm
SnO_2	40nm
PCBM	10nm

$FA_{0.83}Cs_{0.17}Pb(Br_{0.7}I_{0.3})_3$	350nm
Spiro-OMeTAD	250nm
PEDOT:PSS	15nm
ITO Nanoparticles:PCBM 75:25 Effective Medium	50nm
PCBM	80nm
$MAPbI_3$	530nm
Spiro-OMeTAD	180nm
Ag	100nm

$FA_{0.83}Cs_{0.17}Pb(Br_{0.7}I_{0.3})_3$/$MAPbI_3$ (optimized) - Figure C,D

We cap the thicknesses of the non-perovskite layers at 50nm. We add a MgF_2 anti-reflecting coating. We optimize the thicknesses of the perovskite layers and the anti-reflecting coating using a differential evolution algorithm to maximize the limiting current.

The electrical characteristics of the $FA_{0.83}Cs_{0.17}Pb(Br_{0.7}I_{0.3})_3$ are from our own device (Fig S3). The characteristics of the $MAPbI_3$ are from the best cell $MAPbI_3$ in literature.[23] The dotted JV curve models the performance of the tandem assuming the front cell electrically performs as well as current state-of-the-art in Perovskites. We follow the approach of Hörantner et al [19] for this, and assume $EQE_{EL} = 0.01$, $R_S = 4 \cdot 10^{-2}\ \Omega\, cm^2$ and $R_{SH} = 10M\Omega\, cm^2$.

Layer	Thickness
MgF_2	Search space: 10-500nm Optimized: 104nm
Glass	2.2mm
FTO	50nm
SnO_2	40nm
PCBM	10nm
$FA_{0.83}Cs_{0.17}Pb(Br_{0.7}I_{0.3})_3$	Search space: 100-1500nm Optimized: 381nm
Spiro-OMeTAD	50nm
PEDOT:PSS	15nm
ITO Nanoparticles: PCBM 75:25 Effective Medium	50nm
PCBM	50nm
$MAPbI_3$	Search space: 100-1500nm Optimized: 1382nm

Spiro-OMeTAD	50nm
Ag	100nm

$FA_{0.83}Cs_{0.17}Pb(Br_{0.7}I_{0.3})_3/MAPbI_3/MA_{0.4}FA_{0.6}Pb_{0.4}Sn_{0.6}I_3$ triple-junction simulation (optimized)
The calculations for figures E,F are performed exactly as for figures C,D. For the dotted triple junction JV curve, both the front and rear cells are modelled as current state-of-the-art perovskite cells.

Layer	**Thickness**
MgF_2	Search space: 10-500nm Optimized: 92.8nm
Glass	2.2mm
FTO	50nm
SnO_2	40nm
PCBM	10nm
$FA_{0.83}Cs_{0.17}Pb(Br_{0.7}I_{0.3})_3$	Search space: 100-1500nm Optimized: 296.7nm
Spiro-OMeTAD	50nm
PEDOT:PSS	15nm
ITO Nanoparticles:PCBM 75:25 Effective Medium	50nm
PCBM	50nm
$MAPbI_3$	Search space: 100-1500nm Optimized: 583.3
Spiro-OMeTAD	50nm
PEDOT:PSS	15nm
ITO Nanoparticles:PCBM 75:25 Effective Medium	50nm
PCBM	50nm
$MA_{0.4}FA_{0.6}Pb_{0.4}Sn_{0.6}I_3$	Search space: 100-1500nm Optimized: 1382.4
Spiro-OMeTAD	50nm
Ag	100nm

References

[1] Snaith HJ. How should you measure your excitonic solar cells? Energy Environ Sci 2012;5:6513. doi:10.1039/c2ee03429h.

[2] Rossbauer S, Müller C, Anthopoulos TD. Comparative Study of the N-Type Doping Efficiency in Solution-processed Fullerenes and Fullerene Derivatives. Adv Funct Mater 2014;24:n/a-n/a. doi:10.1002/adfm.201401842.

[3] Wang Z, McMeekin DP, Sakai N, van Reenen S, Wojciechowski K, Patel JB, et al. Efficient and Air-Stable Mixed-Cation Lead Mixed-Halide Perovskite Solar Cells with n-Doped Organic Electron Extraction Layers. Adv Mater 2017;29:1604186. doi:10.1002/adma.201604186.

[4] Kim SS, Bae S, Jo WH. Performance enhancement of planar heterojunction perovskite solar cells by n-doping of the electron transporting layer. Chem Commun 2015;51:17413–6. doi:10.1039/C5CC05253J.

[5] Wei P, Menke T, Naab BD, Leo K, Riede M, Bao Z. 2-(2-Methoxyphenyl)-1,3-dimethyl-1 *H* -benzoimidazol-3-ium Iodide as a New Air-Stable n-Type Dopant for Vacuum-Processed Organic Semiconductor Thin Films. J Am Chem Soc 2012;134:3999–4002. doi:10.1021/ja211382x.

[6] Naab BD, Guo S, Olthof S, Evans EGB, Wei P, Millhauser GL, et al. Mechanistic Study on the Solution-Phase n-Doping of 1,3-Dimethyl-2-aryl-2,3-dihydro-1 *H* -benzoimidazole Derivatives. J Am Chem Soc 2013;135:15018–25. doi:10.1021/ja403906d.

[7] Wei P, Oh JH, Dong G, Bao Z. Use of a 1 *H* -Benzoimidazole Derivative as an *n* -Type Dopant and To Enable Air-Stable Solution-Processed *n* -Channel Organic Thin-Film Transistors. J Am Chem Soc 2010;132:8852–3. doi:10.1021/ja103173m.

[8] Noel NK, Habisreutinger SN, Wenger B, Klug MT, Hörantner MT, Johnston MB, et al. A low viscosity, low boiling point, clean solvent system for the rapid crystallisation of highly specular perovskite films. Energy Environ Sci 2017;10:145–52. doi:10.1039/C6EE02373H.

[9] Nguyen WH, Bailie CD, Unger EL, McGehee MD. Enhancing the Hole-Conductivity of Spiro-OMeTAD without Oxygen or Lithium Salts by Using Spiro(TFSI) $_2$ in Perovskite and Dye-Sensitized Solar Cells. J Am Chem Soc 2014;136:10996–1001. doi:10.1021/ja504539w.

[10] Centurioni E. Generalized matrix method for calculation of internal light energy flux in mixed coherent and incoherent multilayers. Appl Opt 2005;44:7532. doi:10.1364/AO.44.007532.

[11] Jain A, Kapoor A. Exact analytical solutions of the parameters of real solar cells using Lambert W -function. Sol Energy Mater Sol Cells 2004;81:269–77. doi:10.1016/j.solmat.2003.11.018.

[12] Hadipour A, de Boer B, Blom PWM. Device operation of organic tandem solar cells. Org Electron 2008;9:617–24. doi:10.1016/J.ORGEL.2008.03.009.

[13] K??nig TAF, Ledin PA, Kerszulis J, Mahmoud MA, El-Sayed MA, Reynolds JR, et al. Electrically tunable plasmonic behavior of nanocube-polymer nanomaterials induced by a redox-active electrochromic polymer. ACS Nano 2014;8:6182–92. doi:10.1021/nn501601e.

[14] Ball JM, Stranks SD, Hörantner MT, Hüttner S, Zhang W, Crossland EJW, et al. Optical properties and limiting photocurrent of thin-film perovskite solar cells. Energy Environ Sci 2015;8:602–9. doi:10.1039/C4EE03224A.

[15] Shi D, Adinolfi V, Comin R, Yuan M, Alarousu E, Buin A, et al. Low trap-state density and long carrier diffusion in organolead trihalide perovskite single crystals. Science 2015;347:519–22. doi:10.1126/science.aaa2725.

[16] Gevaerts VS, Koster LJA, Wienk MM, Janssen RAJ. Discriminating between Bilayer and Bulk Heterojunction Polymer:Fullerene Solar Cells Using the External Quantum Efficiency. ACS Appl Mater Interfaces 2011;3:3252–5. doi:10.1021/am200755m.

[17] Filipič M, Löper P, Niesen B, Wolf S De, Krč J, Ballif C, et al. CH3NH3PbI3 perovskite / silicon tandem solar cells: characterization based optical simulations. Opt Express 2015;23:A263--A278. doi:10.1364/OE.23.00A263.

[18] Johnson PB, Christy RW. Optical Constants of the Noble Metals. Phys Rev B 1972;6:4370–9. doi:10.1103/PhysRevB.6.4370.

[19] Hörantner MT, Leijtens T, Ziffer ME, Eperon GE, Christoforo MG, McGehee MD, et al. The Potential of Multijunction Perovskite Solar Cells. ACS Energy Lett 2017;2:2506–13. doi:10.1021/acsenergylett.7b00647.

[20] Löper P, Stuckelberger M, Niesen B, Werner J, Filipič M, Moon S-J, et al. Complex Refractive Index Spectra of $CH_3NH_3PbI_3$ Perovskite Thin Films Determined by Spectroscopic Ellipsometry and Spectrophotometry. J Phys Chem Lett 2015;6:66–71. doi:10.1021/jz502471h.

[21] Shin SS, Yeom EJ, Yang WS, Hur S, Kim MG, Im J, et al. Colloidally prepared La-doped BaSnO 3 electrodes for efficient , photostable perovskite solar cells 2017;6620.

[22] Prasanna R, Gold-Parker A, Leijtens T, Conings B, Babayigit A, Boyen HG, et al. Band Gap Tuning via Lattice Contraction and Octahedral Tilting in Perovskite Materials for Photovoltaics. J Am Chem Soc 2017;139:11117–24. doi:10.1021/jacs.7b04981.

[23] Shin SS, Yeom EJ, Yang WS, Hur S, Kim MG, Im J, et al. Colloidally prepared La-doped BaSnO3electrodes for efficient, photostable perovskite solar cells. Science 2017;356:167–71. doi:10.1126/science.aam6620.